















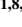




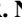







## RESEARCH ARTICLE

10.1029/2023JA031288

# Variability of the Auroral Footprint of Io Detected by *Juno*-JIRAM and Modeling of the Io Plasma Torus

### Key Points:

- *Juno*-JIRAM detected evidence of variability in the Io footprint that are not related to the System III longitude of Io
- Quantitative information on the state of the Io Plasma Torus and its variability are inferred from the Io footprint position
- The Io Plasma Torus electron density varies between  $<2,000$  and  $\sim 2,750$   $\text{cm}^{-3}$ , while the thermal ion temperature varies between 40–100 eV

A. Moirano<sup>1,2</sup> , A. Mura<sup>1</sup> , B. Bonfond<sup>3,4</sup> , J. E. P. Connerney<sup>5</sup> , V. Dols<sup>6</sup> , D. Grodent<sup>3,4</sup> , V. Hue<sup>7</sup> , J.-C. Gérard<sup>3,4</sup> , F. Tosi<sup>1</sup> , A. Migliorini<sup>1</sup> , A. Adriani<sup>1</sup> , F. Altieri<sup>1</sup> , C. Castagnoli<sup>1,8,9</sup> , A. Cicchetti<sup>1</sup> , B. M. Dinelli<sup>8</sup> , D. Grassi<sup>1</sup> , M. L. Moriconi<sup>1</sup> , R. Noschese<sup>1</sup> , G. Piccioni<sup>1</sup> , C. Plainaki<sup>10</sup> , P. Scarica<sup>1</sup> , G. Sindoni<sup>10</sup> , R. Sordini<sup>1</sup> , D. Turrini<sup>1</sup> , and F. Zambon<sup>1</sup> 

<sup>1</sup>Institute for Space Astrophysics and Planetology, National Institute for Astrophysics (INAF—IAPS), Rome, Italy, <sup>2</sup>Sapienza University of Rome, Rome, Italy, <sup>3</sup>Laboratory for Planetary and Atmospheric Physics, Space Science, Technologies and Astrophysical Research Institute, University of Liège, Liège, Belgium, <sup>4</sup>Space Sciences, Technologies and Astrophysics Research Institute, Université de Liège, Liège, Belgium, <sup>5</sup>Space Research Corporation, Annapolis, MD, USA, <sup>6</sup>Laboratory for Atmospheric and Space Physics, University of Colorado Boulder, Boulder, CO, USA, <sup>7</sup>Southwest Research Institute, San Antonio, TX, USA, <sup>8</sup>Institute of Atmospheric Sciences and Climate, National Research Council (CNR - ISAC), Bologna, Italy, <sup>9</sup>University of Rome Tor Vergata, Rome, Italy, <sup>10</sup>Italian Space Agency (ASI), Rome, Italy

### Correspondence to:

A. Moirano,  
alessandro.moirano@inaf.it

### Citation:

Moirano, A., Mura, A., Bonfond, B., Connerney, J. E. P., Dols, V., Grodent, D., et al. (2023). Variability of the auroral footprint of Io detected by *Juno*-JIRAM and modeling of the Io Plasma Torus. *Journal of Geophysical Research: Space Physics*, 128, e2023JA031288. <https://doi.org/10.1029/2023JA031288>

Received 2 JAN 2023  
Accepted 1 AUG 2023

**Abstract** One of the auroral features of Jupiter is the emission associated with the orbital motion of its moon Io. The relative velocity between Io and the surrounding plasma trigger perturbations that travels as Alfvén waves along the magnetic field lines toward the Jovian ionosphere. These waves can accelerate electrons into the atmosphere and ultimately produce an auroral emission, called the *Io footprint*. The speed of the Alfvén waves—and hence the position of the footprint—depends on the magnetic field and on the plasma distribution along the field line passing through Io, whose SO<sub>2</sub>-rich atmosphere is the source of a dense plasma torus around Jupiter. Since 2016, the Jovian InfraRed Auroral Mapper (JIRAM) onboard *Juno* has been observing the Io footprint with a spatial resolution of  $\sim$ few tens of km/pixel. JIRAM detected evidences of variability in the Io footprint position that are not dependent on the System III longitude of Io. The position of the Io footprint in the JIRAM images is compared with the position predicted by a model of the Io Plasma Torus and of the magnetic field. This is the first attempt to retrieve quantitative information on the variability of the torus by looking at the Io footprint. The results are consistent with previous observations of the density and temperature of the Io Plasma Torus. However, we found that the plasma density and temperature exhibit considerable non-System III variability that can be due either to local time asymmetry of the torus or to its temporal variability.

## 1. Introduction

The auroral activity on Jupiter is the most intense among the planets in the Solar System (Grodent, 2015), thanks to the strong planetary magnetic field, the fast rotation of Jupiter and the dense plasma environment of its magnetosphere. Indeed, the volcanic moon Io injects  $\sim 1$  ton  $\text{s}^{-1}$  of material (e.g., Kivelson et al., 2004), which is the source of a dense plasma cloud around Io's orbit, called *Io Plasma Torus* (IPT). The signature of the strong Jovian aurorae is detected at various wavelengths: radio (Kurth et al., 2017; Zarka, 1998), infrared (Drossart et al., 1989; Trafton et al., 1989), visible (Gladstone et al., 2007; Ingersoll et al., 1998; Vasavada et al., 1999), ultraviolet (Caldwell et al., 1992; Clark & Mc Cord, 1980; Dols et al., 1992; Grodent et al., 2006; Livengood et al., 1992; Skinner et al., 1984) and X-ray (Dunn et al., 2020; Gladstone et al., 2002; Yao et al., 2021). The morphology of the Jovian aurorae is complex and includes distinct features, like the local emissions associated with the Jovian moons—called *footprints*. The footprints were largely detected equatorward of the main aurora for Io (Clarke et al., 1996; Connerney et al., 1993; Prangé et al., 1996), Europa and Ganymede (Clarke et al., 2002), while only one observation is reported for Callisto (Bhattacharyya et al., 2018). These features originate from the relative velocity between the magnetospheric plasma and the moons, where the local perturbation in the plasma flow excites electromagnetic modes such as Alfvén and magnetosonic waves that propagates away from the satellite (Acuña et al., 1981; Belcher et al., 1981; Neubauer, 1980; Saur, 2004). In particular, the Alfvén waves travel along the magnetic field lines toward the Jovian atmosphere. As the Alfvén waves propagate toward the planet, they can accelerate electrons into the ionosphere by wave-particle interaction (Damiano et al., 2019; Hess et al., 2010; Jones & Su, 2008; Lysak & Song, 2003), eventually producing the auroral footprints (Miller et al., 2020). The Alfvén speed depends on both the magnetic field and plasma density along the field lines, therefore the position

©2023. The Authors.

This is an open access article under the terms of the [Creative Commons Attribution License](https://creativecommons.org/licenses/by/4.0/), which permits use, distribution and reproduction in any medium, provided the original work is properly cited.

of the footprint can be used to derive quantitative information about the magnetospheric environment at the magnetic shells of the moons. The goal of the present work is to use the high-resolution images of the Io footprint (IFP) acquired by the Jovian InfraRed Auroral Mapper (JIRAM) (Adriani et al., 2017) onboard *Juno* (Bolton et al., 2017) to detect variations in the IFP position that are not due to the orbital motion of the satellite, but (potentially) to variations in their surrounding plasma environment. The JIRAM observations are then used to derive quantitative information on the plasma distribution in the IPT, such as density and temperature. The variability of the IPT is a long-lasting topic of research (Brown, 1995), with two major questions: (a) how the IPT changes depending on the Iogenic source (e.g., Roth et al., 2020) and (b) how the Jovian magnetosphere responds to the variability of the torus (e.g., Bonfond, Hess, Bagenal, et al., 2013). To properly address these issues, it is essential to simultaneously and continuously monitor Io, the IPT and the aurorae. In the present work, we show that the observations of the IFP can be used to constrain the plasma properties of the IPT and to point out variations of the plasma torus. This will help ground based observations and in situ measurements reconstruct the evolution of the IPT and its interplay with Io and the Jovian magnetosphere.

The IPT mainly consists of  $S^{2+}$  and  $O^+$  ions (Broadfoot et al., 1979; Kupo et al., 1976; Sandel et al., 1979). Due to the tilt of the Jovian magnetic dipole axis with respect to the spin axis by  $\sim 10^\circ$  toward  $\sim 200^\circ$  System III longitude (in the following, longitudes will be tacitly referred to System III), the fast rotation of the magnetosphere confines the plasma around the centrifugal equator, that is: the furthest points from the planetary spin axis along the magnetic field lines (Hill et al., 1974; Phipps et al., 2020). Consequently, the tilt of the centrifugal equator relative to the Jovian equator is approximately 2/3 of the magnetic dipole tilt, that is about  $7^\circ$ . The material in the IPT is mainly supplied by the constantly ongoing volcanic activity of the moon and by sublimation of  $SO_2$  from the surface (Roth et al., 2020; Tsuchiya et al., 2018, 2019). The IPT can be divided into three regions—the inner disk, the ribbon and the warm torus—by the physical and chemical properties of the plasma (Bagenal & Dols, 2020). Io's orbit is located at  $5.9 R_J$  ( $1 R_J = 71,492$  km), hence it orbits within the warm torus for most of the time, but the ribbon can occasionally approach Io's orbit, due to the local time variation of the torus (Schneider & Trauger, 1995). At Io's orbit, the warm torus has a typical thickness of  $\sim 1 R_J$  and electron density of  $\sim 2,000$   $cm^{-3}$  (Bagenal, 1994; Bagenal et al., 1997; Bagenal & Sullivan, 1981; Moirano, Gomez Casajus, et al., 2021; Phipps et al., 2021). Due to the high density of the warm torus and the weak equatorial magnetic field at Io's orbit relative to the field at the planet surface, the Alfvén waves travels at a few hundreds  $km s^{-1}$  within the IPT, while they propagate at a significant fraction of the speed of light in the low density region between the torus and the ionosphere (Hinton et al., 2019). The Alfvén waves propagating along the field lines form a stationary structure in Io's frame, called an *Alfvén Wing* (Drell et al., 1965; Neubauer, 1980) and its foot is the location of Io's auroral footprint. The Alfvén wings form an angle with the magnetic field given by  $\tan(\alpha) = v_{flow}/v_A$ , where  $v_{flow}$  is the plasma speed relative to Io and  $v_A$  is the Alfvén speed (Equation 1).

The IFP can be described as a series of bright *spots* separated by a few thousands kilometers and a fading *footprint tail* (Bonfond et al., 2008). This morphology reflects the complex pattern of the Alfvén waves (see Figure 1): some spots can be ascribed to the Alfvén waves coming from the moon itself (the *Main Alfvén Wing spot* or MAW), some others from the multiple reflections of the waves on Alfvén speed gradients (the *Reflected Alfvén Wing spot* or RAW), such as at the transition between the high-density IPT and the low-density high-latitude magnetosphere or near the ionosphere (Hess et al., 2010; Jacobsen et al., 2007). At times, it is also possible to observe a leading spot, depending on Io's centrifugal latitude in the torus. This emission is attributed to field-aligned electrons accelerated in the Main Alfvén Wing toward the opposite Jovian hemisphere and is called the *Transhemispheric Electon Beam spot* (TEB). The relative positions of the MAW, the RAW and the TEB spots change as Io orbits Jupiter because of the change in Io's centrifugal latitude (Bonfond, 2012; Bonfond, Grodent, et al., 2017; Gérard et al., 2006). Besides, *Juno*-JIRAM recently revealed an additional small-scale structure, which is called *sub-dots* to avoid confusion with the MAW-RAW-TEB spots (Moirano, Mura, et al., 2021; Mura et al., 2018). The typical separation between the sub-dots is 200–300 km and it was suggested that they originate from an ionospheric feedback that triggers the production of additional Alfvén waves from the ionosphere (Moirano, Mura, et al., 2021), reflections of Alfvén waves between the ionosphere and the IPT (Schlegel & Saur, 2022) and variations in the conductivity of the Jovian ionosphere (Lysak et al., 2021).

The warm torus exhibits both temporal and spatial variabilities, which can be roughly classified into four categories, namely: (a) System III longitude variations, (b) System IV longitude variations, (c) temporal variations due to the variable plasma mass loading from Io and (d) dusk-dawn asymmetries (see Bagenal and Dols (2020) for an extensive review on the Io torus).

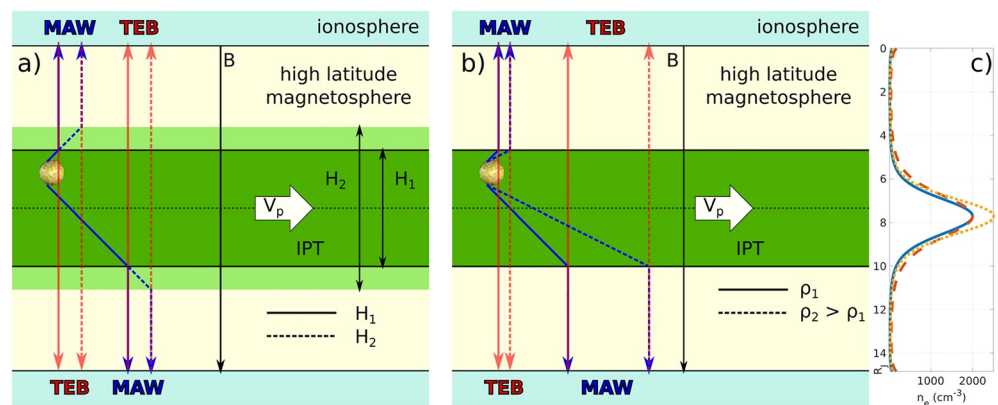


**Figure 1.** Sketches of the Alfvén wings in Io's rest frame when the moon is above the centrifugal equator (black dotted line) under different plasma distributions. The plasma in the IPT (green area) flows from left to right as specified by the white arrow. The density of the torus is assumed uniform in the sketch. The magnetic field is also uniform and points southwards (black arrow). The light blue areas are the Jovian ionospheres where auroral emissions occur. *Panel (a):* Alfvén wings for two different sizes of the IPT with the same density. The torus thickness is represented by  $H_1$  (dark green) and  $H_2 > H_1$  (light green). The blue solid arrows represent the path of the Alfvén waves when the thickness of the IPT is  $H_1$ , while the blue dashed ones the path when the thickness is  $H_2$ . The red arrows point out the path of the field-aligned TEB in the two conditions. *Panel (b):* Alfvén wings for two values of the density ( $\rho_1$  and  $\rho_2 > \rho_1$ ), while the size of the torus is the same. The reflected Alfvén wings are not drawn for sake of clarity. *Panel (c)* shows examples of three more realistic electron density distributions, computed using the diffusive equilibrium model (Bagenal & Sullivan, 1981) described in Section 3. The vertical axis is the distance along the magnetic field line crossing the orbit of Io at  $0^\circ$  longitude, measured from the northern hemisphere. The blue and red dashed lines correspond to the case in panel (a), and the blue and orange dotted lines to panel (b).

System III variations are detected in the infrared (IR) and ultraviolet (UV) wavelengths (Lichtenberg et al., 2001; Sandel & Broadfoot, 1982a) and they are associated with the configuration of the Jovian magnetic field and its period of  $\sim 9.9$  hr (Chenette et al., 1974). In System III, the IPT shows  $\sim 5\%$  azimuthal variations in electron density and  $\sim 10\%$  in electron temperature (Steffl et al., 2006). This variability can be explained by heating by Alfvén waves and the longitudinal variation of the mirror ratio of the magnetic field (Hess et al., 2011).

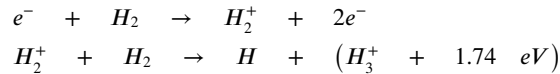
System IV variations are associated with a longitudinal modulation of the plasma composition that shows a periodicity  $\sim 1\%–5\%$  slower than System III (Kaiser & Desch, 1980; Roesler et al., 1984; Sandel & Dessler, 1988; Steffl et al., 2006). Modeling efforts revealed that this modulation might be associated with a small fraction of hot electrons (Hess et al., 2011; Steffl et al., 2008) ( $\sim 0.2\%$  of the total electron content, with a temperature of  $\sim 55$  eV) as well as to local sub-corotation of plasma between 6 and  $7 R_J$  (Copper et al., 2016).

Temporal variations of the plasma content of the IPT result from neutrals lost from Io's atmosphere, which is sustained by a combination of volcanic output (very variable) and  $\text{SO}_2$  frost sublimation (Koga et al., 2019; Roth et al., 2020; Tsuchiya et al., 2019). As the contribution of each process is still highly debated, the resulting variation of the torus plasma content is very difficult to address, both with observations and modeling. The IPT variations rely on the interplay between atmospheric mass loss from Io, supply of neutrals to the neutral clouds that extend along Io's orbit, plasma mass loading of the torus and radial transport, and the resulting magnetospheric response. Volcanic activity on Io may take different forms, like calderae, explosive and flow-dominated eruptions and plumes (Davies, 2001; Lopes & Williams, 2015), and each of them can provide a different amount of gas and dust with different timings. Besides, the location of these events on Io's surface can affect the effective mass loading of the IPT (McDoniel et al., 2019). Furthermore, the new material from Io affects the properties of the atmosphere and ionosphere of the moon, which ultimately interacts with the IPT, affecting the effective mass loading of plasma, neutrals and dust into the Jovian magnetosphere (Delamere et al., 2004; Hikida et al., 2020; Koga et al., 2019; Yoneda et al., 2010, 2013). In order to properly address the temporal variability of the IPT, it is necessary to monitor all these elements.

The local time asymmetry refers to the radial displacement of the torus toward the dawnside by  $\sim 0.2 R_J$  and the higher brightness of the dusk ansa compared to dawn ansa (Morgan, 1985; Schneider & Trauger, 1995). A candidate explanation for this local time asymmetry is the plasma flow in Jupiter's magnetotail, which sets up

a magnetospheric electric field from dawn to dusk (Barbosa & Kivelson, 1983; Ip & Goertz, 1983). This field pushes the torus further from Jupiter on the dawn side and compresses the torus on the duskside, which explains the enhanced brightness observed in this latter region (Murakami et al., 2016).

The *Juno* spacecraft entered the Jupiter system in August 2016 and since then it performed over 40 orbits around the planet. The geometry of its trajectory is polar and highly eccentric, so *Juno* has a unique vantage point for observing the polar regions of Jupiter (Bagenal et al., 2017). JIRAM L-band imager, whose observations will be the backbone throughout the present work, covers the 3.3–3.6  $\mu\text{m}$  range, where the emission from  $\text{H}_3^+$  ions can be detected with a good contrast against the sunlit planetary disc. These ions are a byproduct of the electron precipitation (Miller et al., 2020; Wu et al., 2019):



where the  $\text{H}_3^+$  retains 1.74 eV of internal energy that is subsequently radiated as IR emission (Oka, 1980). The emission is expected to occur above 500 km from the 1-bar pressure level, as at lower altitude the  $\text{H}_3^+$  is rapidly destroyed by its reaction with methane (Gérard et al., 2018; Grodent et al., 2001).

In the present work, we survey the first 40 orbits of *Juno* to report evidence of variations in the IFP position. System III variations due to Io wiggling up and down within the IPT will not be covered here, as they are already documented in the literature (e.g., Bonfond et al., 2008; Bonfond, Grodent, et al., 2017). Instead, we aim at finding evidence of System IV variations, as well as temporal and local time variations. Variations in the morphology of the Io (Bonfond, Hess, Gérard, et al., 2013) and Ganymede footprints (Bonfond, Hess, Bagenal, et al., 2013) at the same System III longitude were observed by the *Hubble Space Telescope* and it was suggested that they reflect the variability of the plasma environment around the satellites. In the present work, we move a step forward by deriving quantitative information on the IPT conditions at different epochs. To address the present investigation, we will specifically focus on the positions of the MAW and TEB, in order to avoid the complex pattern of reflections of Alfvén waves that takes place along the footprint tail as far as possible.

The data set used in the present study is introduced in Section 2. Section 3 explains the model used for mapping Io's instantaneous position to its auroral footprint in Jupiter's ionosphere. The comparison between data and model is presented in Section 4, while a discussion of the results is given in Section 5. Conclusions are in Section 6.

## 2. Observations and Data Reduction

The bulk of the data used in the present study comes from the observations performed by the JIRAM L-band imager that covers the 3.3–3.6  $\mu\text{m}$  band. JIRAM has a spatial resolution of  $\sim 0.01^\circ$ , corresponding to a few tens kilometers on average at the ionosphere: this allows the detection of small details in the auroral emissions. Images acquired with this filter are affected by the interference from the adjacent M-filter operating in the 4.5–5.0  $\mu\text{m}$  band and designed to observe the planetary atmosphere (Adriani et al., 2017, 2018). To correct the images, an empirical background of the form  $A(x)e^{-\frac{y}{B}} + C$  was constructed, where  $x$  and  $y$  are the columns and rows of the detector respectively ( $y = 0$  is the closest row to the M-filter), while  $A(x)$ ,  $B$  and  $C$  are best fit parameters computed for each image (Mura et al., 2017). The subtraction of this empirical background helps to retrieve the morphology of the footprints, but slightly affects the intensity. This effect is particularly evident near the junction between the two filters, where the background gradually conceals all the auroral emissions. Therefore, the first 38 rows near the M-filter were removed.

The altitude of the emission needs to be taken into account in order to accurately determine the coordinates of the emissions. Based on auroral emission models, the peak altitude of the IR emission is expected to occur between 500 and 1,000 km for electron energies between 0.1 and 100 keV (Tao et al., 2011). *Juno*-JADE-E electron measurements (McComas et al., 2017) reported a broadband electron energy distribution associated with the IFP, with a peak energy between 0.1 and 1 keV (Sulaiman et al., 2020; Szalay et al., 2020), which implies that the IR emission should peak near 900–1,000 km. JIRAM observed the IFP during both perijoves (PJ) 4 and 7 in the northern hemisphere when its longitude was between  $\sim 90^\circ$  and  $120^\circ$  at two different emission angles (i.e., the angle between the normal to the planetary surface and the line of sight from the instrument). This allows to retrieve the altitude of the footprint by stereoscopy, and it is estimated to peak at  $600 \pm 100$  km. Potentially, this discrepancy stems from the assumption of a maxwellian distribution for the electrons in the model by Tao et al. (2011), while

JADE-E measurements reported a kappa distribution. The difference between the two distributions is stronger at higher energy: the maxwellian one underestimates the contribution of high energy electrons, which penetrate deeper into the atmosphere and cause the emission to occur at lower altitudes.

The images acquired during the first 42 orbits of *Juno* were surveyed to report evidences of variability of the IFP. In this study, we focus on two specific features of the IFP to constrain the plasma properties of the IPT, that are the MAW and the TEB, because (a) they can be easily identified, especially when the TEB is located upstream of MAW and (b) they are less affected by the complex pattern of the reflected Alfvén waves that develops along the footprint tail (Bonfond, Saur, et al., 2017). In order to be selected for the present analysis, the images should meet three criteria. First, the footprint has to be observed during two or more orbits with Io in nearly the same System III longitude: this requirement rules out variability due to System III variations, allowing the detection of the other types of variability, as summarized in Section 1. Second, JIRAM performs multiple sequences of images during every flight over the poles and the images are taken 30 s apart from each other. The IFP moves at  $\sim 2.5\text{--}6\text{ km s}^{-1}$  relative to Jupiter in the North and  $\sim 3\text{--}4.5\text{ km s}^{-1}$  in the South, which implies that it moves by about 100–150 km between two subsequent images. Hence, it is essential to restrict the analysis to single images or—if not possible—to tessellations of 2–3 consecutive images in order to limit the effect of the movement of the emission. Therefore, both the MAW and the TEB spots should be identifiable in the same sequence or, better, in the same image, so that their relative distance can be used to highlight any potential variability. Lastly, images showing the TEB leading the MAW are better suited for the retrieval of the position of these spots than observations with the TEB downstream. Indeed, the brightness of the sub-dots can interfere with the morphology of the TEB, making more difficult the determination of the precise location of TEB spot when it is downstream. Nevertheless, the TEB emission can still be detected as a brightness envelope that affects the emission of a group of sub-dots toward the tail (see Figure 3 in Moirano, Mura, et al., 2021). The sub-dots show a typical spacing of  $\sim 200\text{--}300\text{ km}$ , which should be taken into account to estimate the position of the TEB.

The data set used in this work consists of images taken over the southern hemisphere and it is divided in two pairs of observations: PJ 10–31 (16 December 2017 at UTC 19:51 and 30 December 2020 at UTC 23:21, respectively) and PJ 11–32 (7 February 2018 at UTC 15:55 and 21 February 2021 at UTC 19:28, respectively). The difference in Io's longitude between the images in each of these pairs is less than  $1.5^\circ$ .

### 3. Models of the Io Plasma Torus and the Magnetic Field

Comparing the JIRAM data set with a model of the plasma distribution in the IPT to predict the position of the MAW and TEB spots serves a dual purpose: retrieving quantitative information about the plasma and highlighting differences between different observations. As introduced in Section 1, the flow perturbation at Io produces an Alfvén wave that travels away from the moon and toward the planetary ionosphere along the magnetic field lines. This disturbance propagates at the Alfvén speed

$$v_A = \frac{B}{\sqrt{\mu_0 \rho}} \quad (1)$$

where  $B$  is the magnitude of the magnetic field,  $\rho$  is the ion mass density and  $\mu_0$  is the magnetic permeability in vacuum. Near Io's orbit, the magnetic field is weaker than above the ionosphere of Jupiter ( $\sim 2,000\text{ nT}$  (Kivelson et al., 2004) versus  $\sim 10^6\text{ nT}$  (Connerney et al., 2022)), while the plasma density is higher in the IPT than in the high-latitude magnetosphere ( $\sim 1,000\text{--}2,000\text{ cm}^{-3}$ , mainly  $\text{O}^+$  and  $\text{S}^{2+}$  (Bagenal, 1994), versus  $\sim 10\text{--}100\text{ cm}^{-3}$ , mainly  $\text{H}^+$  and ionized states of O and S (Huscher et al., 2021)). Therefore, the Alfvén speed is minimum within the IPT (150–340 km/s; see Kivelson et al., 2004) and approaches the speed of light when the alfvénic perturbation reaches the Jovian ionosphere. Because of the very strong magnetic field of Jupiter, the Alfvén speed must be corrected for relativistic effect in the high-latitude magnetosphere, hence:

$$v_A^{rel} = \frac{v_A}{\sqrt{1 + \left(\frac{v_A}{c}\right)^2}} \quad (2)$$

where  $c$  is the speed of light. As the alfvénic perturbation travels along the magnetic field lines, the time  $t_A$  required to reach the ionosphere from Io is given by the integration of the Alfvén speed along the given field line. During the same time  $t_A$  Io continues its orbital motion, hence it is possible to build a map that relates Io's position with the MAW spot at any given time. For this purpose, a magnetic field model and a plasma density distribution are required to compute the Alfvén speed defined in Equation 1. Additionally, the position of the TEB

spot can be computed by mapping the position of the MAW spot in the opposite hemisphere along the magnetic field (Bonfond et al., 2008; Jacobsen et al., 2010), as its energetic electrons quickly travel along the magnetic field lines between the two hemispheres in <30 s (Hess et al., 2013). For comparison, the Alfvén travel time associated with the MAW spot is between 2 and 12 min, depending on the distance of Io from the centrifugal equator (Hinton et al., 2019).

The *Juno* reference magnetic field model, built from the first 33 *Juno* orbits (JRM33, from Connerney et al. (2022)) is used to compute the internal magnetic field. For consistency with the footprints provided in the supporting information of Connerney et al. (2022), the spherical harmonic expansion of the field is limited at degree 18. We also take into account the magnetic contribution of the current in the plasmadisk by including the magnetodisk formulation of Connerney et al. (2020).

The plasma density in the IPT is computed using a diffusive equilibrium model (Bagenal & Sullivan, 1981; Mei et al., 1995; Thomas, 1992), which takes into account the electron and ion pressures, the centrifugal and gravitational forces, the magnetic mirror force and the ambipolar electric field due to charge separation driven by the centrifugal motion of the plasma. Assuming that the temperature of the ions and electrons is constant along the field lines, the density distribution of the species  $\alpha$  along each field line is given by

$$n_{\alpha}(s) = n_{\alpha 0} \exp \left[ \frac{m_{\alpha} \Omega_J^2 (\rho^2 - \rho_0^2)}{2k_B T_{\alpha \parallel}} + \frac{m_{\alpha}}{k_B T_{\alpha \parallel}} G M_J \left( \frac{1}{r} - \frac{1}{r_0} \right) + \left( 1 - \frac{T_{\alpha \perp}}{T_{\alpha \parallel}} \right) \ln \left( \frac{B}{B_0} \right) - Z_{\alpha} e \frac{\Delta \phi(s)}{k_B T_{\alpha \parallel}} \right] \quad (3)$$

where  $m_{\alpha}$  is the particle mass,  $\Omega_J$  the angular rotation of Jupiter,  $k_B$  is the Boltzmann constant,  $T_{\alpha \parallel}$  and  $T_{\alpha \perp}$  are the parallel and perpendicular temperatures respectively,  $G$  the gravitational constant,  $M_J$  the Jovian mass,  $r$  and  $\rho$  the distance from the planet center and spin axis respectively,  $B$  the magnetic field magnitude,  $Z_{\alpha}$  the atomic number ( $Z_{\alpha} = -1$  for the electrons),  $\Delta \phi = \phi(s) - \phi_0$  the potential drop associated with the ambipolar electric field,  $s$  the distance from the centrifugal equator along the field line. The quantities denoted with “0” refer to the centrifugal equator. For the electrons, the centrifugal and gravitational terms (the first two on the rhs of Equation 3) can be neglected because of their small mass compared to the mass of the ions. Besides, for species with isotropic temperatures ( $T_{\alpha \parallel} = T_{\alpha \perp}$ ) the mirror force (i.e., the third term on the rhs of Equation 3) can be omitted. The temperature anisotropy of the thermal ions is expected to be  $1 \leq T_{\alpha \perp}/T_{\alpha \parallel} < 2$ , while the hot ions can exhibit higher values ( $3 < T_{\alpha \perp}/T_{\alpha \parallel} < 10$ , see Cray et al., 1996, 1998). Assuming that the electrons have isotropic temperatures, the density of each species can be derived by solving the following system:

$$n_e(s) = n_{e0} \exp \left[ e \frac{\Delta \phi(s)}{k_B T_{e \parallel}} \right] \quad (4)$$

$$n_i(s) = n_{i0} \exp \left[ \frac{m_i \Omega_J^2 (\rho^2 - \rho_0^2)}{2k_B T_{i \parallel}} + \frac{m_i}{k_B T_{i \parallel}} G M_J \left( \frac{1}{r} - \frac{1}{r_0} \right) + (1 - A_{\alpha}) \ln \left( \frac{B}{B_0} \right) - Z_i e \frac{\Delta \phi(s)}{k_B T_{i \parallel}} \right] \quad (5)$$

$$n_e(s) = \sum_i Z_i n_i(s) \quad (6)$$

where the subscripts  $e$  and  $i$  stands for electrons and ions respectively and  $A_{\alpha} = T_{\alpha \perp}/T_{\alpha \parallel}$ . Equation 6 is the condition of charge neutrality, which couples Equations 4 and 5.

The plasma composition used as reference in the present work is based on the re-analysis of the *Voyager 1* data by Dougherty et al. (2017). The reference value for the electron density  $n_{e0}$  at the intersection of the centrifugal equator with the magnetic shell of Io is  $2,500 \text{ cm}^{-3}$ . Eight ion species are included in the model and their densities are computed from the electron density and the ion mixing ratios (i.e., the ion-to-electron density ratios) at  $6 R_J$ :  $\text{H}^+$  (1%),  $\text{O}^+$  (24%),  $\text{O}^{2+}$  (3%),  $\text{S}^+$  (7%),  $\text{S}^{2+}$  (22%),  $\text{S}^{3+}$  (3%),  $\text{Na}^+$  (3%) and  $\text{O}_{hot}^+$  (6%). The electron and ion temperatures are also taken at  $6 R_J$  (5 eV for electrons, 94 eV for protons, 80 eV for  $\text{O}^+$ ,  $\text{O}^{2+}$ ,  $\text{S}^+$ ,  $\text{S}^{2+}$ ,  $\text{S}^{3+}$  and  $\text{Na}^+$ , 362 eV for  $\text{O}_{hot}^+$ ). To study different plasma distributions, we compute several electron density distributions derived from equatorial

**Table 1**  
Summary of the Parameter Space of the Sensitivity Test of Section 3

| Case | $S_T^a$ | $n_{e0}^b$ | $H^{+c}$ | $T_{H^+}^d$ | $A_{th}^e$ | $O_h^{+c}$ | $A_{O_h^+}^e$ | O <sup>+</sup> S <sup>+</sup> S <sup>2+</sup> S <sup>3+</sup> <sup>c</sup> | Na <sup>+</sup> O <sup>2+</sup> <sup>c</sup> |
|------|---------|------------|----------|-------------|------------|------------|---------------|--|--|
| 1    | 1.00    | 2,500      | 1        | 94          | 1          | 6          | 6.5           | 24, 7, 22, 3   | 3, 3   |
| 2a   | 0.50    | -          | -        | -           | -          | -          | -             | -  | -  |
| b    | 0.75    | -          | -        | -           | -          | -          | -             | -  | -  |
| c    | 1.25    | -          | -        | -           | -          | -          | -             | -  | -  |
| d    | 1.50    | -          | -        | -           | -          | -          | -             | -  | -  |
| 3a   | -       | 2,000      | -        | -           | -          | -          | -             | -  | -  |
| b    | -       | 2,250      | -        | -           | -          | -          | -             | -  | -  |
| c    | -       | 2,750      | -        | -           | -          | -          | -             | -  | -  |
| d    | -       | 3,000      | -        | -           | -          | -          | -             | -  | -  |
| 4a   | -       | -          | 0        | -           | -          | -          | -             | 25,-,-,-   | -  |
| b    | -       | -          | 10       | -           | -          | -          | -             | 21,-,20,-  | 1,-  |
| 5a   | -       | -          | -        | 50          | -          | -          | -             | -  | -  |
| b    | -       | -          | -        | 150         | -          | -          | -             | -  | -  |
| 6a   | -       | -          | 10       | 50          | -          | -          | -             | 21,-,20,-  | 1,-  |
| b    | -       | -          | 10       | 150         | -          | -          | -             | 21,-,20,-  | 1,-  |
| 7    | -       | -          | -        | -           | 2          | -          | -             | -  | -  |
| 8    | -       | -          | -        | -           | -          | 0          | -             | 30,-,-,-   | -  |
| 9a   | -       | -          | -        | -           | -          | -          | 1             | -  | -  |
| b    | -       | -          | -        | -           | -          | -          | 3             | -  | -  |
| c    | -       | -          | -        | -           | -          | -          | 10            | -  | -  |
| 10a  | -       | -          | -        | -           | -          | -          | -             | 23,9,23,2  | -  |
| b    | -       | -          | -        | -           | -          | -          | -             | 20,11,25,1   | -  |
| c    | -       | -          | -        | -           | -          | -          | -             | 25,5,21,4  | -  |
| d    | -       | -          | -        | -           | -          | -          | -             | 28,3,19,5  | -  |
| 11   | 0.50    | 3,000      | 0        | /           | -          | 0          | /             | 42,26,16,0   | 0,0  |

Note. Empty spaces should be referred to Case 1.

<sup>a</sup>The ion temperatures are reported in term of the scaling factor  $S_T$ . <sup>b</sup>Electron density in  $\text{cm}^{-3}$ . The ion densities are derived from the mixing ratios of Section 3. <sup>c</sup>The abundance of the ions are in mixing ratio  $\frac{n_{\alpha}}{n_e}$ . <sup>d</sup>Temperature, in eV. <sup>e</sup>Anisotropy  $A_{\alpha} = T_{\alpha\perp}/T_{\alpha\parallel}$ .  $A_{th}$  is for the thermal ions,  $A_{O_h^+}$  for the hot oxygen.

values  $n_{e0}$  between 2,000 and 3,000  $\text{cm}^{-3}$  with steps of 250  $\text{cm}^{-3}$ . This interval is consistent with previous observations of the IPT (Bagenal & Dols, 2020; Delamere & Bagenal, 2003; Moirano, Gomez Casajus, et al., 2021; Phipps et al., 2021; Thomas et al., 2004), although occasional more extreme cases were detected. The ion density distributions are computed from the above-mentioned mixing ratios, estimated from *Voyager 1* (Dougherty et al., 2017). Past observations of the IPT constrained the ion temperature within a factor 2 (Thomas, 1995); moreover, volcanic events are followed by a temperature increase up to a factor 3 (Delamere et al., 2004). Therefore, we explore different ion temperatures by scaling the *Voyager 1* observations at Io's orbit by a factor  $S_T$  ranging from 0.50 to 1.50 with 0.25 steps. The thermal ion and electron temperatures are assumed isotropic (Crary et al., 1998), while for the hot oxygen  $A_{O_h^+} = 6.5$  (i.e., the average of the values reported by Crary et al. (1996)). A summary of the above-mentioned parameters is presented in Table 1 (Case 1, 2 and 3).

## 4. Results

In the following section we present the results of the model described in Section 3 alongside the observations introduced in Section 2. As each ion density is computed from the equatorial value of the electron density, we present the results in terms of the equatorial electron density  $n_{e0}$ . The corresponding ion densities can be calculated according to the ion fractions in Section 3 and Table 1. The present section is further divided into two subsections. First, we test the sensitivity of the model to various parameters in order to determine which ones mostly affect the position of the footprint. Then we compare the model with the IFP observed during PJ 10, 11, 31 and 32 in order to show evidence of variability of its position.

In the following, we call *reference model* the plasma distribution corresponding to Case 1 in Table 1, obtained by setting  $n_{e0} = 2,500 \text{ cm}^{-3}$ ,  $S_T = 1.00$ ,  $A_i = 1$  for the thermal ions,  $A_{O^+_{hot}} = 6.5$  and the mixing ratios described at the end of Section 3.

### 4.1. Sensitivity Tests

The plasma distribution in the Io plasma torus depends on many parameters, according to Equations 4 and 5. To properly address the variability of the IFP position, we first need to determine which of these parameters is the most influent. Therefore, in the current section we investigate the sensitivity of the model output to the following parameters: peak electron density  $n_{e0}$ , ion temperatures  $T_{ij}$ , proton mixing ratio, proton temperature  $T_{H^+}$ , temperature anisotropy of the thermal ions, inclusion of the hot oxygen population, temperature anisotropy of the hot oxygen and different mixing ratios of  $O^+$ ,  $S^+$ ,  $S^{2+}$  and  $S^{3+}$ . Additionally, as Io can potentially enter the ribbon near the dawn ansa, we test a ribbon-like plasma distribution. In Table 1 (case 2–11) we summarized the parameters used for the sensitivity test.

In the top panel of Figure 2 we report the one way Alfvén travel time, that is: the time the Alfvén waves take to travel from Io to the North or South hemisphere. The one-way travel time predicted by our reference model is between 4 and 14 min, 1.5 min longer than the model of Hinton et al. (2019). This difference may stem from the different magnetic model used in the present work as well as from a different choice for the ion mixing ratios and temperatures. Indeed, the ion temperature shows a sharp drop from  $6 R_J$  inwards: if we use  $S_T = 0.75$  in our model, this improves the agreement with the results from Hinton et al. (2019), the difference between the two models being 0.7 min.

In the bottom panel of Figure 2 we report the percent difference of the Alfvén travel time obtained from cases 2–10 with respect to the reference Case 1. To compute the percentage, we first compute the travel time  $t_{ref}$  with Io at  $290^\circ$  longitude (i.e., approximately in the centrifugal equator) for the reference model, and the travel time  $t$ , obtained by changing one parameter at a time. Then the percentage is obtained from  $(t_{ref} - t)/t_{ref}$ . Hence a positive/negative percentage represents a faster/slower travel time.

*Ion Temperature Scaling (Case 2).* We scale the ion temperature by a factor  $S_T$  between 0.50 and 1.50, which changes the Alfvén travel time between +20% and –15%. Indeed, changes in the temperature affect the size of the Io plasma torus, therefore by increasing/decreasing the temperature at a constant peak density  $n_{e0}$ , the total plasma content along the magnetic field lines increases/decreases as well. Consequently, the Alfvén travel time is reduced/increased.

*Peak Electron Density (Case 3).* The electron density at the centrifugal equator  $n_{e0}$  is varied between 2,000 and 3,000  $\text{cm}^{-3}$ , which correspond to a time travel variation between +10% and –10%. This is not surprising, as the Alfvén speed depends on the reciprocal of the square root of the ion mass density, which is proportional to the electron density and the ion mixing ratios. Therefore lower/higher density implies faster/slower Alfvén waves.

To understand why changes in  $S_T$  and  $n_{e0}$  produce a similar effect on the Alfvén travel time  $t_A$ , we can estimate  $t_A$  from the simple geometry of Figure 1. Assuming uniform magnetic field  $B_0$ , mass density  $\rho_0 = \text{constant} > 0$  in the IPT and  $\rho_0 = 0$  outside (not to be confused with the cylindrical radius in Equation 5), the travel time is given by



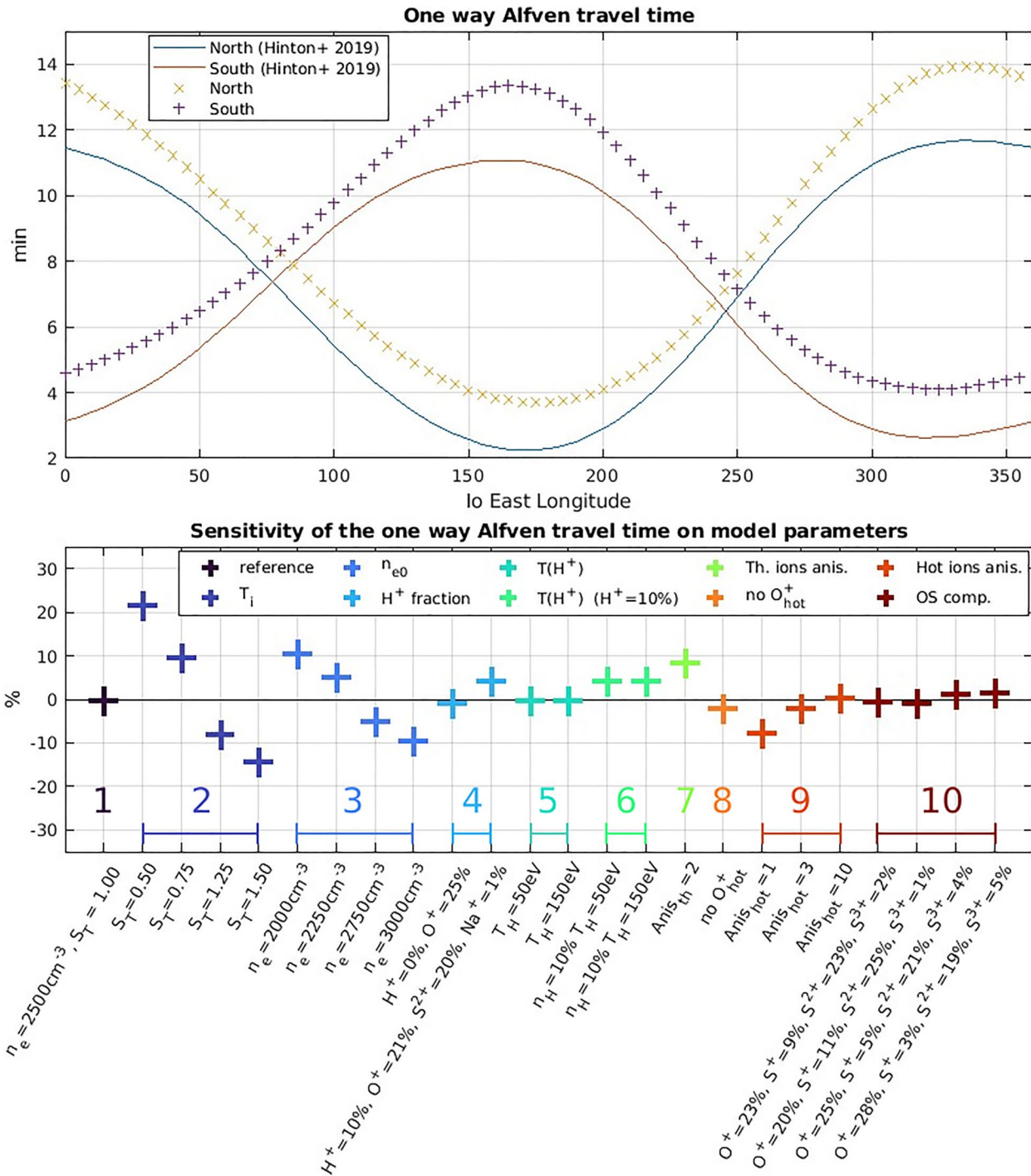


**Figure 2.** Top: One way Alfvén travel time predicted by the *Voyager 1* reference model of Section 3 from Io to the North (orange crosses) and South hemisphere (purple pluses) respectively. The blue and red lines are the travel times reported by Hinton et al. (2019). Bottom: sensitivity of the one way Alfvén travel time calculated when Io is close to the centrifugal equator in the warm torus at System III longitude 290°. The numbering from 1 to 10 points to the cases in Table 1 and the labels on the x axis briefly specify the values used for the test. The percentage represents how much faster the Alfvén wave travels compared to the reference, therefore a positive/negative value implies a shorter/longer travel time.

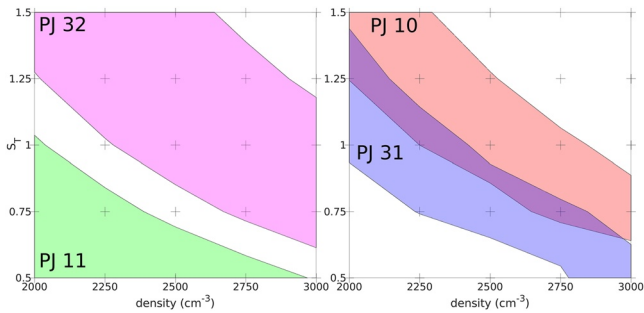


**Figure 3.** Parameter space obtained for PJ 11 and 32 (left side) and PJ 10 and 31 (right side). The colored areas represent the parameter spaces that predict the MAW spot position within 250 km for each JIRAM observations.

$$t_A = \int_{s_{Io}}^{s_{iono}} \frac{ds}{v_A} = \int_{s_0}^{s_{iono}} \frac{\sqrt{\mu_0 \rho(s)}}{B(s)} ds \approx \frac{\sqrt{\mu_0 \rho_0}}{B_0} \Delta L \quad (7)$$

where  $\Delta L$  is the distance traveled by the Alfvén wave in the region where  $\rho_0 > 0$ ,  $s_{Io}$  and  $s_{iono}$  are the positions of Io and the planetary ionosphere along a magnetic field line respectively.  $\Delta L$  can be expressed in terms of the thickness of the IPT ( $H$  in Figure 1), which in turn depends roughly on the square root of the ion temperature (Bagenal & Sullivan, 1981), hence:  $\Delta L \sim H \sim \sqrt{T_i}$ . Therefore we obtain

$$t_A \propto \sqrt{\rho_0 T_i} \quad (8)$$

which explains why the travel time increases or decreases with both density and temperature. Because the position of the footprint is determined by  $t_A$ , there is a degeneracy between  $n_{e0}$  and  $S_T$ . This can be seen by looking at the parameter space derived for PJ 10–31 and PJ 11–32 in Figure 3, where we report the values of  $n_{e0}$  and  $S_T$  that predict the MAW spot position within 250 km from the JIRAM observations (this value is approximately half the longitudinal size of the MAW spot). The regions of the parameter space compatible with the observations have an hyperbolic shape, which agrees with Equation 8.

**Proton Mixing Ratio (Case 4).** Due to the light mass of the protons compared to the sulfur and oxygen masses, protons are not expected to considerably affect the Alfvén speed within the IPT. Nevertheless, at high latitude, where heavy ions are almost absent, protons dominate the plasma density. The proton abundance in the IPT is 1%–10% (Bodisch et al., 2017; Delamere et al., 2005; Nerney & Bagenal, 2020), hence we increase their mixing ratio to 10% (case 4b). In order to preserve charge neutrality, we have to decrease the mixing ratios of  $O^+$ ,  $S^{2+}$  and  $Na^+$  (see Table 1 and the labels in Figure 2 for the quantitative details). Besides, we also completely remove the protons to investigate the role of their presence (case 4a), although there is no observational evidence of a complete hydrogen depletion in the IPT. By removing the protons from the ion species,  $t_A$  decrease by less than 1%, while by increasing their mixing ratio to 10%  $t_A$  increases by about 4%. This changes are not due to the variations of the proton mixing ratio itself, but rather to the adjustment made to the other mixing ratios. Indeed, the Alfvén speed in the high latitude magnetosphere is still a large fraction of the speed of light even for a 10% proton mixing ratio and the Alfvén waves spend a few tens of seconds in the low density region between the IPT and the Jovian ionosphere.

**Proton Temperature (Case 5 and 6).** To determine the role of the spatial distribution of  $H^+$ , we test a proton temperature of 50 and 150 eV, which approximately corresponds to the scaling of the reference value 94 eV by  $S_T = 0.5$  and 1.50 respectively. The resulting  $t_A$  is the same as the one obtained with the reference temperature of 94 eV within 10<sup>-5</sup>%. In order to amplify any possible effect on  $t_A$ , we also tested the same temperatures with a 10% proton mixing ratio: the travel time changes by only ~0.05% with respect to the case with the same mixing ratio at  $T_{H^+} = 94$  eV. Indeed, protons are loosely confined by the centrifugal force because of their light mass and thus they spread quite uniformly along the magnetic field lines. Therefore, changes in their temperature affect very little their distributions.

**Temperature Anisotropy of the Thermal Ions (Case 7).** We set  $A_i = 2$ , according to the results reported in Cray et al. (1996), to determine the effect of the magnetic mirror force confinement on the thermal ions. This value reduces  $t_A$  by about 9%. Indeed, the confinement reduces the size of the IPT, hence the total plasma content along the field lines decreases as well, reducing the Alfvén travel time.

**Presence of Hot  $O^+$  and Its Temperature Anisotropy (Case 8 and 9).** In situ measurement of the IPT revealed the presence of  $O^+$  ions with a temperature of ~400 eV (Dougherty et al., 2017). To probe the effect of such population on the position of the IFP, we compared the reference model against a model with only thermal oxygen (Case 8). This increases  $t_A$  by less than 2%. Indeed, the distributions of the hot and thermal oxygen populations have a typical thickness of ~2  $R_J$  and they peak at about 0.3  $R_J$  from each other along the magnetic field lines, as they are confined near the magnetic and centrifugal equator, respectively. Therefore, they largely overlap and the case with no hot oxygen has a similar mass distribution as the reference model. To assess the importance of the magnetic mirror force confinement, we test the case  $A_{O^+_{hot}} = 1$  (isotropy, case 9a),  $A_{O^+_{hot}} = 3$  (low anisotropy, case 9b) and

$A_{O^+_{hot}} = 10$  (high anisotropy, case 9c). The first case is used to determine the effect of the inclusion of anisotropy in Equation 3, while the other two test the lower and upper limit on the anisotropy reported by *Voyager 1* (Crary et al., 1996). The changes of  $t_A$  are  $-8\%$ ,  $-2\%$  and  $+0.5\%$ , respectively. In the case of isotropic temperature, the hot oxygen distribution is broadly distributed along the field lines, and it is the dominant species by density at high latitude. Thus, the Alfvén waves are slower at high latitude with respect to the reference case and the travel time is longer. The cases with low and high anisotropy are quite close to the reference, which suggest that the position of the IFP is little sensitive on the precise value of  $A_{O^+_{hot}}$ . Nevertheless, the inclusion of the temperature anisotropy of the hot oxygen is relevant for proper modeling (i.e.,  $A_{O^+_{hot}} > 1$  in Equation 5).

*Mixing Ratios of  $O^+$ ,  $S^+$ ,  $S^{2+}$  and  $S^{3+}$  (Case 10)*. The azimuthal distribution of  $O^+$  and  $S^{2+}$  in the IPT fluctuates by  $2\%$ – $5\%$ , depending on the relative phase between System III and System IV (Hess et al., 2011; Steffl et al., 2008), while for  $S^+$  and  $S^{3+}$  the fluctuations are  $5\%$ – $25\%$  (Steffl et al., 2006). Besides, the mixing ratio of  $S^+$  is correlated with the mixing ratio of  $S^{2+}$ , while it is anti-correlated with  $O^+$  and  $S^{3+}$ . We test two different set of the  $O^+$ ,  $S^+$ ,  $S^{2+}$  and  $S^{3+}$  mixing ratios that are roughly compatible with the amplitude variations associated with System IV (Case 10a and 10c). Besides, we test two arbitrarily large variations of  $O^+$  correlated with  $S^{3+}$  and anticorrelated with  $S^+$  and  $S^{2+}$  (Case 10b and 10d). These are not supported by observational or modeling evidences and they are included for the sole purpose of the sensitivity test. In all the above-mentioned cases the variation of  $t_A$  is smaller than  $2\%$ . The most abundant sulfur ion (i.e.,  $S^{2+}$ ) has the same charge-to-mass ratio as the most abundant oxygen ion (i.e.,  $O^+$ ), hence, for the same electron density, the total mass in the IPT changes mostly due to the variation in the  $S^+$  and  $S^{3+}$ . Therefore, the change of  $t_A$  caused by the increase/decrease of the  $O^+$  and  $S^{3+}$  mixing ratios is compensated by the decrease/increase of the  $S^+$  and  $S^{2+}$  mixing ratios.

*Ribbon (Case 11)*. The ribbon exhibits higher electron density and a slightly lower temperature than the warm torus, as well as considerably different mixing ratios. To test the potential effect of the ribbon on the MAW spot position, which might occur when Io is near the dawn ansa, we set  $n_{e0} = 3,000 \text{ cm}^{-3}$  and  $S_T = 0.5$  (Bagenal & Dols, 2020), while for the mixing ratios of the major ions  $O^+$ ,  $S^+$  and  $S^{2+}$  we used  $42\%$ ,  $26\%$  and  $16\%$ , respectively (Bagenal, 1994). The travel time in this case is  $5\%$  longer than the reference case (not shown in Figure 2). This suggest that a longer  $t_A$  from the IFP observations near the dawn ansa could be explained by the ribbon moving near Io. In the present study, we do not aim at deriving the plasma parameters at the ribbon, which has its own parameter space to be tested and investigated. Nevertheless, a relatively high density derived near the dawn ansa in the present study might be interpreted as the ribbon approaching Io's orbit.

## 4.2. Data-Model Comparison

Following the results of the sensitivity test of the previous section, we now compare the results of the model of Section 3 with the position of the IFP observed by JIRAM. The focus will be on the peak electron density  $n_{e0}$  and the ion temperature through the scaling factor  $S_T$ . In Section 4.1 and Figure 2 we showed that the temperature anisotropy is also a relevant parameter for both the thermal and hot ion populations. Nevertheless, the value of the anisotropy is poorly determined from the literature. Besides, the diffusive equilibrium model Equations 4–6 is based on the assumption of constant temperature along the field line, while it likely increases at high latitude (Thomas & Lichtenberg, 1997). Thus, the temperature anisotropy may also change along the magnetic field lines. Lastly, in Section 4.1 we showed that including an anisotropy  $A_{O^+_{hot}} > 1$  in Equation 5 is more important than a precise value for  $A_{O^+_{hot}}$ . For these reasons, we decided to postpone an in-depth analysis of the anisotropy effect on the IFP position to a future work, which will also include the latitudinal variation of the temperature. In the present study we therefore assume that the temperature of the thermal ions is isotropic, while for the hot oxygen  $A_{O^+_{hot}} = 6.5$ .

Each image of the footprint is compared to the location of the footprint calculated from  $n_{0e} = 2,500 \text{ cm}^{-3}$  and  $S_T = 1.00$ , which serves as the *Voyager 1*-based reference, and we test different values for the density and for the temperature, as explained at the end of Section 3. In Figure 3 we show the parameter spaces compatible with the observed positions of the MAW spot within  $250 \text{ km}$  (i.e., the distance between the observed and predicted position of the spot is less than  $250 \text{ km}$ ). In the case of PJ 11–32, the parameter spaces are not compatible, PJ 11 preferring lower temperatures and densities than PJ 32. The parameter space of PJ 10 covers slightly higher temperatures and densities than PJ 31, but the two spaces are marginally compatible.

Figure 4 shows the JIRAM observations performed during PJ 10–31 (panel *a*) and 11–32 (panel *b*), when the TEB spot was upstream of the MAW spot. We superimpose colored pluses and crosses that represent the modeled positions of these two auroral features to the images, according to different values of the electron density and the ion temperature. To highlight the respective role of the density and the temperature, we show the predicted position of the MAW spot by varying only one parameter at a time from the reference case. The position of the MAW and TEB spots predicted by the *Voyager 1* values are represented by asterisks. In panel *a* Io was at the same longitude  $\phi_{Io} = 205.2^\circ$ , but the images show that the MAW spot of PJ 31 was at a higher longitude by  $\sim 1^\circ$  than PJ 10. This displacement corresponds to about 300 km on the surface of Jupiter. The emission angle was  $\sim 10^\circ$  in both cases, therefore the error associated with the emission altitude of  $600 \pm 100$  km translates to an uncertainty on the position of the MAW of  $< 20$  km along the track of the IFP. Hence, it is unlikely that the displacement between the images results from the uncertainty of the emission. By comparing the modeled position of the MAW spot in the left column of panel *a* in Figure 4 (colored pluses), we conclude that the best match corresponds to the ion distribution obtained from an electron density of about  $2,500\text{--}2,750\text{ cm}^{-3}$  for PJ 10 and  $2,000\text{--}2,250\text{ cm}^{-3}$  for PJ 31, while the best match temperature (right column) is determined by  $S_T = 1.00\text{--}1.25$  and  $0.75$  respectively.

During the PJ 11 and 32 observations shown in panel *b* of Figure 4, Io was at  $169.4^\circ$  and  $170.8^\circ$  longitude respectively. The position of the MAW spot differs by less than 100 km in the two images; besides, it is clear that the distance between the tip of the TEB and the MAW in each image is remarkably different in the two orbits ( $\sim 1,000$  km and  $\sim 1,700$  km respectively). The emission angle for PJ 11 was  $\sim 20^\circ$ , which translates to an uncertainty of less than 40 km on the IFP position, while for PJ 32 the angle was  $\sim 5^\circ$ , corresponding to an uncertainty smaller than 10 km. This noticeable morphological difference is reflected in the model prediction: the electron density of PJ 11 was likely smaller than  $2,000\text{ cm}^{-3}$ , while for PJ 32 it is significantly different at  $n_{e0} \approx 2,750\text{ cm}^{-3}$ . The best fit scaling factor for the temperature during these two orbits is  $S_T = 0.50$  and  $1.25$  for PJ 11 and 32 respectively.

In Table 2 we summarize the results of the present section for PJ 10–31 and 11–32.

## 5. Discussion

In Section 4.1 we showed that the IFP position predicted by the model of Section 3 depends mostly on the plasma density and ion temperature. The temperature anisotropy is also important, even though we suggest that determining if  $A_i = 1$  or  $A_i \neq 1$  in Equation 5 is more important than having a precise value. For this reason and because of the poor constraints currently available on this parameter from the literature, we decided to assume that the temperature of the thermal ions is isotropic, while for the hot ions we set an anisotropy of 6.5, according to the *Galileo*-based results in Crary et al. (1996, 1998). Therefore, in the following, we focus the discussion on the density and temperature retrieved from the present model (Table 2) and the JIRAM images (Figure 4), while we do not discuss the anisotropy any further.

### 5.1. Comparison With Previous Missions, *HISAKI* and *Juno*

The density and temperature of the IPT were previously constrained mainly by spectroscopy from both ground-based facilities (e.g., Schmidt et al., 2018) and in situ missions (e.g., Steffl et al., 2008). Additional sources of observations are radiocollations (e.g., Bird et al., 1993) and direct particle measurements (e.g., Bagenal & Sullivan, 1981). In the following, we show how the results obtained from the IFP position compare with those from other measurements.

*Voyager 1* The ion plasma composition of the inner magnetosphere of Jupiter measured by the *Voyager 1* Plasma Science instrument (PLS) re-analyzed by Dougherty et al. (2017) is the reference point of the present analysis, therefore it is a straightforward comparison with the *Juno*-JIRAM measurements. The electron density we report in Table 2 differs by about  $\pm 250\text{ cm}^{-3}$  with respect to the *Voyager 1* value of  $2,450\text{ cm}^{-3}$  at  $6 R_J$ , except during PJ 11, when the best fit density was smaller than  $2,000\text{ cm}^{-3}$ . The temperature measured by *Voyager 1* steeply increases from 2 to 3 eV to  $\sim 80$  eV between 5 and  $6 R_J$ . The temperature used in the reference model is the one measured by *Voyager* at  $6 R_J$ , which might overestimate the value at  $5.9 R_J$  by  $\sim 10$  eV. The best fit temperature in the present analysis corresponds to a temperature scaling factor  $S_T$  between 0.75 and 1.25, except for PJ 11, whose best match is  $S_T = 0.50$ . Therefore, the IPT density variations inferred from the IFP position in JIRAM data is about 10% the density measured by *Voyager 1*, while the temperature changes by about 25%.

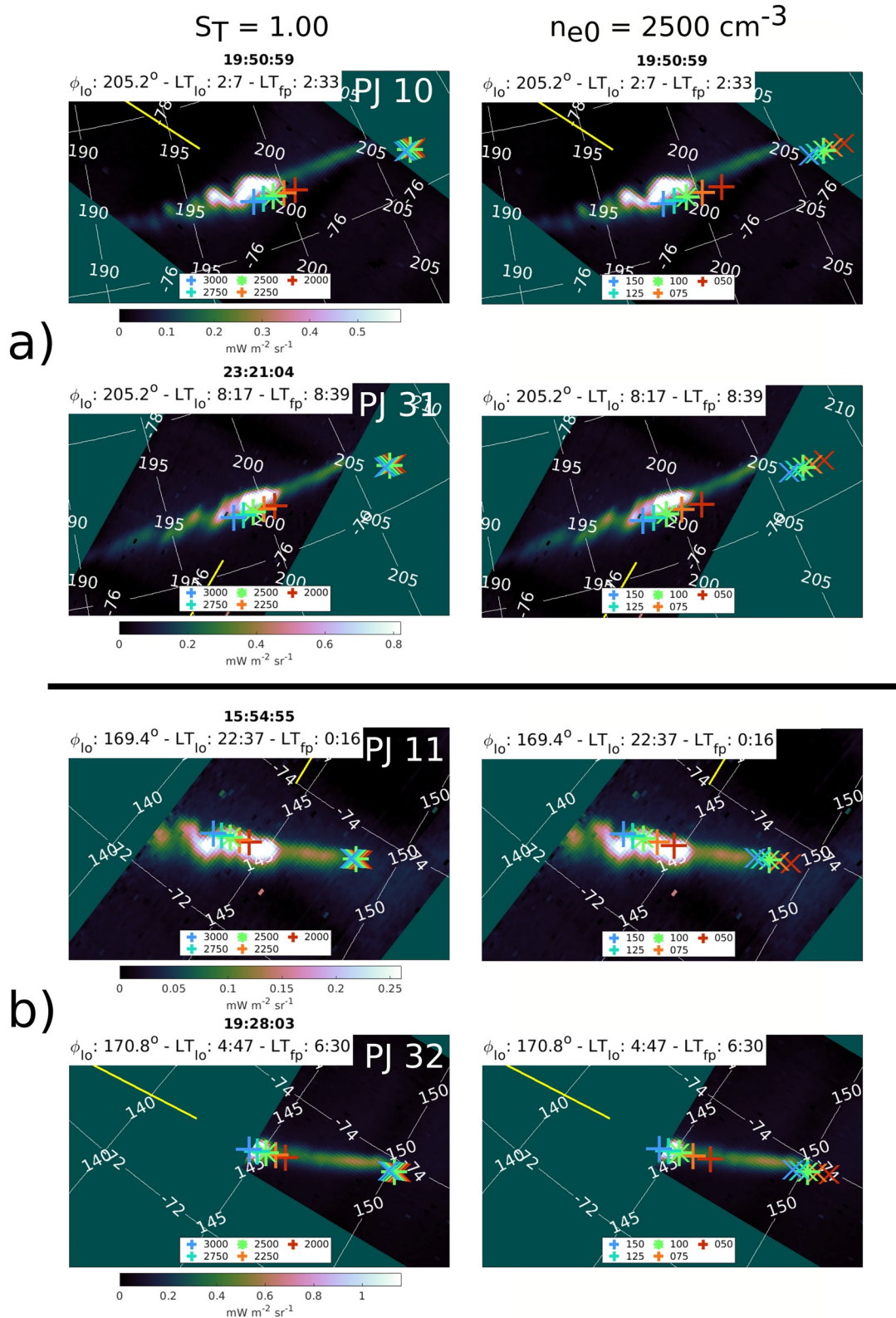


**Figure 4.** Comparison between JIRAM data and the model of Section 3 for PJ 10–31 (panel a) and PJ 11–32 (panel b). The pluses and the crosses represent the predicted position of the MAW and TEB respectively. The position of the MAW and TEB for the reference model ( $n_{e0} = 2500 \text{ cm}^{-3}$  and  $S_T = 1.00$ ) is represented by an asterisk. The yellow line is aligned with the MAW-Sun direction. The left column shows the predicted position of the MAW and TEB spots for  $n_{e0}$  between 2,000 and 3,000  $\text{cm}^{-3}$  for constant  $S_T = 1.00$ , while the right column the prediction for  $S_T$  between 0.50 and 1.50 for  $n_{e0} = 2,500 \text{ cm}^{-3}$ . UTC time is reported in the titles in the left column, while Io System III longitude and local time of both Io and the IFP are reported in each figure.

**Table 2**  
Summary of the Best-Match Electron Density and Ion Temperature

| PJ | $\phi_{III}$ (deg) | Io local time (hh:mm) | $n_{e0}$ (cm <sup>-3</sup> ) <sup>a</sup> | $S_T$ <sup>b</sup> |
|----|--------------------|-----------------------|---|--------------------|
| 10 | 205.2              | 02:07                 | 2500–2750                                 | 1.00–1.25          |
| 31 | 205.2              | 08:17                 | 2000–2250                                 | 0.75               |
| 11 | 169.4              | 22:37                 | <2000                                     | 0.50               |
| 32 | 170.8              | 04:47                 | 2750                                      | 1.25               |

<sup>a</sup>The ion densities assume  $S_T = 1.00$ . <sup>b</sup>The ion temperatures scaling factor assume  $n_{e0} = 2,500$  cm<sup>-3</sup>.

*Voyager 1*, *Voyager 2* and *Cassini* Delamere and Bagenal (2003) investigated the variability of the IPT using a chemistry model that depends on the radial transport time, the source of neutral particles, the oxygen-to-sulfur ratio and the fraction and temperature of the hot electrons. Their results were then compared with observations of the IPT performed by *Voyager 1*, *Voyager 2* and *Cassini*. They found remarkable differences in the torus properties between those missions: the electron density was 1,800–2,200 cm<sup>-3</sup> for *Voyager 1*, 2,600–3,400 cm<sup>-3</sup> for *Voyager 2* and 1,700–2,000 cm<sup>-3</sup> for *Cassini*. The density we derived from PJ 10, 11, 31 and 32 are compatible with these values for the different epochs. The density of PJ 10 and 32 is compatible with the density observed during *Voyager 2*, the density of PJ 31 with the observations of *Voyager 1* and the density of PJ 11 with the measurements of *Cassini*. It is interesting that the IPT might have lost 25%, and

potentially more, of its electron density from PJ 10 to PJ 11 in only ~50 days. Nerney and Bagenal (2020) used a chemistry model to investigate the plasma properties of the IPT and compared the expected spectral emission with the observations made by *Cassini*-UVIS. The electron density in that work is ~1,900 cm<sup>-3</sup>, while the ion temperature is 60–70 eV for S<sup>2+</sup>, S<sup>3+</sup>, O<sup>+</sup> and O<sup>2+</sup> (corresponding to  $S_T \sim 0.75$  in the present model), ~100 eV for S<sup>+</sup> (corresponding to  $S_T \sim 1.25$ ) and ~90 eV for the protons. Therefore the electron density and temperature we obtained for PJ 11 and 31 suggest that the IPT was in a state similar to that observed during the *Cassini* epoch rather than during the *Voyager 1* and *Voyager 2* epochs.

*Juno* The *Juno* spacecraft performed several radio occultations of the IPT thanks to the Ka-band Translator System (KaTS) and the Small Deep Space Transponder (SDST). These occultations probe directly the total electron content (TEC) between the spacecraft and the ground station (Bertotti et al., 1993), thus they can be used to determine the electron content of the IPT. By analyzing the radio occultations from PJ 1 to 15, Phipps et al. (2021) reported that the maximum TEC of the warm torus is 24 hexem on average (1 hexem = 10<sup>16</sup> electrons m<sup>-2</sup>) and varies between 17 and 29 hexem. Moirano, Gomez Casajus, et al. (2021) analyzed the radio occultations from PJ 1 to 25, assuming that the radial density distribution of the warm torus outside 5.5 R<sub>J</sub> can be modeled by a Gaussian profile  $N \exp\left[-\frac{(r-R)^2}{W^2}\right]$ , with  $R = 5.7 R_J$  and  $W = 1.5 R_J$ , while  $N$  is a free parameter for the peak electron density. The electron density reported in that analysis is ~2,500 cm<sup>-3</sup> on average, with variations between 1,400 cm<sup>-3</sup> and 3,400 cm<sup>-3</sup>. These large variations in electron density based on *Juno* radio occultations are roughly compatible with the different torus conditions observed during *Voyager 1* (~2,000–2,500 cm<sup>-3</sup>), *Voyager 2* (~2,600–3,400 cm<sup>-3</sup>) and *Cassini* (~1,700–2,000 cm<sup>-3</sup>) (Delamere & Bagenal, 2003). The electron density reported in the present study is between <2,000 cm<sup>-3</sup> and 2,750 cm<sup>-3</sup>, in agreement with the results from the radio occultations. More specifically, the radio occultation during PJ 11 showed a remarkably low electron density compared to other orbits, while the torus appeared slightly thicker (Moirano, Gomez Casajus, et al., 2021; Phipps et al., 2021). This suggests that the position of the IFP of PJ 11 in panel *b* of Figure 4 may be explained by a density depletion rather than a temperature drop. PJ 11 showed evidence of strong magnetospheric activity, which was detected by the *Juno* magnetometer as a high number of reconnection events associated with plasmoid ejection in the magnetotail (Vogt et al., 2020). At the same time, both *Juno* and the *Hubble Space Telescope* (HST) reported a dawn storm (Bonfond et al., 2021; Nichols et al., 2020), which are usually associated with large scale magnetotail reconfigurations, but not the global main auroral brightening typically associated with a solar wind compression (Yao et al., 2022). On the other side, Huscher et al. (2021) reported particularly low density in the middle magnetosphere during PJ 12, but not during PJ 11, for which they do not record any remarkable feature. A comprehensive analysis of the above-mentioned datasets to determine the timeline of events of PJ 11 is not the aim of the present work, but the position of the IFP can be used as an additional piece of evidence to pursue that goal.

*Hisaki* and *Cassini* The IPT response to strong volcanic events was studied using the *Cassini* fly by during the period October 2000 - March 2001 (Delamere et al., 2004) and *Hisaki* monitoring from 2013 to 2015 (Yoshioka et al., 2018). By using the *Cassini*-UVIS measurements, Delamere et al. (2004) concluded that the electron density initially decreased from 2,500 cm<sup>-3</sup>–2,200 cm<sup>-3</sup> in about 25 days, and it increased up to 2,700 cm<sup>-3</sup> in the next ~75 days. At the same time, the ion temperature increased from ~50 eV to ~110–140 eV in about 30 days and then it fell back to the pre-event value in the following 30 days. Yoshioka et al. (2018) compared the *Hisaki*-EXCEED spectroscopic observations during a volcanically quiet period (November 2013) with the meas-

measurements of an active period (February 2015). The evolution of the brightness of the torus detected by *Hisaki* was similar to the one observed by *Cassini*, so they suggested that there was a similar trigger (i.e., a major volcanic event) in 2000 and 2015. The electron density estimated during the February 2015 event is  $2,860 \pm 260 \text{ cm}^{-3}$ , to be compared with the density of the quiet period in November 2013 of  $2,350 \pm 340 \text{ cm}^{-3}$ . The brightness enhancement in 2015 lasted for about 3 months, and then it came back to the quiet period level. The density increases observed by *Cassini* and *Hisaki* are similar to the electron density found for PJ 32 and marginally for PJ 10. Major volcanic events such as the ones in 2000 and in 2015 are expected to be quite rare, approximately one every  $\sim 5\text{--}10$  years, even though our knowledge of the frequency of such events is affected by the impossibility of continuous monitoring of Io and the torus. Besides, there are no report of such events since the arrival of *Juno* at Jupiter. Therefore, it appears unlikely that the density reported for PJ 10 and 32 was caused by one of these events.

## 5.2. Causes of Torus Variability and Their Effect on the Io Footprint Position

As discussed in Section 1, the IPT exhibits different types of variability, that is, System III and System IV variations, temporal variations and local time variability (Bagenal & Dols, 2020). This classification is rooted in the underlying physical processes that drive each type of variability, as briefly introduced in Section 1, but there is a mutual influence. For example, mass loading into the IPT can cause a radial displacement of its dawn ansa (Brown & Bouchez, 1997)—thus increasing the dawn-dusk asymmetry—as well as a change in the System IV periodicity (Tsuchiya et al., 2019). System III and System IV modulations create a beat that can be detected in the UV brightness (Steffl et al., 2006). In this section, we discuss each type of variability separately for sake of clarity—bearing in mind the above-mentioned interplay—to explain how the torus variability can affect the IFP and what types of variations are compatible (or detectable) using footprint position. For the cases presented in Figure 4, System III variability can be ruled out, as the observations were performed within a few degrees longitude.

*System IV Variability* System IV variability is difficult to infer from the present data set. In Section 4.1 we tested different ion compositions of the IPT that are correlated with System IV periodicity. The increase of  $\text{O}^+$  and  $\text{S}^{3+}$  at the expense of  $\text{S}^+$  and  $\text{S}^{2+}$  causes a slight decrease of the Alfvén travel time, while  $t_A$  increases in the opposite case. Nonetheless, these changes affect the Alfvén travel time by less than 2%, which implies that the position of the IFP in these cases differs by  $\sim 30$  km with respect to the position predicted by the reference model. This difference is smaller than the difference in the IFP position observed by JIRAM during PJ 10–31 and 11–32 (Figure 4). Therefore, we suggest that System IV variability has a negligible effect on the position of the IFP.

*Local Time Asymmetry* The ribbon region of the torus is located at a radial distance from the spin axis of the planet of  $5.56 \pm 0.07$  on the dusk side and  $5.83 \pm 0.06 R_J$  on the dawn side (Schmidt et al., 2018; Schneider & Trauger, 1995; Smyth et al., 2011). The uncertainty represents the System III modulation of the dawn-dusk asymmetry. The ribbon is  $\sim 0.2 R_J$  wide and has a similar vertical extension as the warm torus, but its density is as high as  $\sim 3,000 \text{ cm}^{-3}$  and it consists mainly of  $\text{O}^+$ ,  $\text{S}^+$  and  $\text{S}^{2+}$  (Bagenal & Dols, 2020). As explained in Section 1, the torus dawn-dusk displacement is usually explained by the presence of a dawn-dusk electric field, which depends on the magnetic field as well as the plasma flow in the magnetotail (Barbosa & Kivelson, 1983) and it might be affected by their dynamics and variability (e.g., Kennel & Coroniti, 1977; Murakami et al., 2016). Therefore, the dawn-dusk asymmetry could be increased or reduced by changes of the plasma flow in the magnetotail. Besides, the direction of the electric field appears to be tilted with respect to the dawn-dusk direction by  $15\text{--}20^\circ$  (Sandel & Broadfoot, 1982b; Smyth et al., 2011), therefore the two ansae occur at 7–7:20 and 19–19:20 hr in local time, instead of at 6 and 18. For each set of observations in Table 2 and Figure 4, one image was acquired near the dawn side between 04:47 and 08:17 local time (i.e., PJ 31 and 32). Nevertheless, those observations do not always correspond to a density increase with respect to the corresponding images taken at the same longitude, which might suggest that Io did not enter the ribbon. Indeed, during PJ 31 (08:17 local time) the best fit density was lower compared to PJ 10 (02:07 local time). On the other hand, PJ 32 (04:47 local time) showed a remarkable density increase compared to PJ 11, which occurred at 22:37 local time. Another interpretation of this results might lie in the variability of the ribbon itself. For example, the Plasma Wave Subsystem onboard *Galileo* reported no signs of the presence of the ribbon along the J0 flyby in December 1995 (Bagenal et al., 1997); instead, the electron density in the same region was only a few hundreds  $\text{cm}^{-3}$  at the typical location of the ribbon, while the electron density at Io orbit was surprisingly large ( $\sim 4,000 \text{ cm}^{-3}$ ). The hypotheses proposed at that time was that either the ribbon was not present or that Io was located in the ribbon at the time of the J0 flyby. The  $n_{e0}$  obtained from PJ 10 and 31 suggests that the ribbon was not present at the time of the PJ 10 observations and that Io was in a transition region between the warm and cold torus. Additionally, the

supply of material from the torus to the magnetosphere can affect the plasma flow in the magnetotail and, hence, the dawn-dusk electric field. It was observed that the dawn ansa shifts dawnward by  $\sim 0.3 R_J$  during periods of increased IPT mass (Brown & Bouchez, 1997), but the dusk ansa remains in place. This effect might have displaced the dawn ansa more dawnward during PJ 32 than PJ 31, so that Io was orbiting within the ribbon at that time; nevertheless simultaneous observations of the IPT are needed to confirm any mass loading events. Furthermore, based on brightness observations of the IPT by *Hisaki*, it was suggested that a solar wind-driven compression of the Jovian magnetosphere can increase the dawn-dusk field, hence shifting the IPT dawnward by  $\sim 0.2 R_J$  (Murakami et al., 2016), although this shift could not be measured simultaneously by *Hisaki* itself. The reliability of solar wind propagation models based on near-Earth measurements decreases near solar conjunction (Zieger & Hansen, 2008) and, at the time of the JIRAM observations reported here, the Jupiter-Sun-Earth angle (JSE) was  $-155^\circ$ ,  $-100^\circ$ ,  $145^\circ$  and  $180^\circ$  for PJ 10, 11, 31 and 32 respectively. Besides, the uncertainty on the timing of compression events from these propagation model is  $\sim 15$  hr during opposition, and rapidly increases with the JSE angle. This, with the limited data set used in this work, prevents a statistical analysis to potentially correlate the solar wind variations with the IPT. Lastly, the density does not increase monotonically from the warm torus to the ribbon. For example, in Figure 6 in Dougherty et al. (2017), the data shows a small dip of a few hundreds  $\text{cm}^{-3}$  between the two regions (called *the gap* (Herbert et al., 2008)), which could be consistent with the results in Table 2.

**Temporal Variability** If the other types of variability can be quite confidently excluded - such as System III and IV in the previous part of this section - or less confidently - such as local time asymmetries - the only other source of variability may lay in the temporal variability of the IPT and its mass loading. Indeed, in principle any variation in the supply of material into the IPT can affect its density and temperature (e.g., Delamere et al., 2004; Yoshioka et al., 2018), which in turn affect  $t_A$  in Equation 7 and thus the position the MAW spot. The loading can be caused by internal or external sources. Internal sources means that the plasma comes from the local interaction between Io, the neutral cloud along its orbit and the magnetospheric environment, while a driving mechanism that lies outside the plasma torus can be referred to as an external source. The volcanic activity on Io is the ultimate internal source. The various types of hot spots (Lopes & Williams, 2015) on Io's surface eject material (such as Na, NaCl, SO<sub>2</sub>, SO and K) that likely do not directly contribute to plasma loading and scatters in Io atmosphere. SO<sub>2</sub> is the dominant species in the atmosphere of the satellite, and it is sustained by either sublimation from the surface or by direct volcanic input (Roth et al., 2020). Both the atmosphere and the ionosphere interact with the plasma environment, providing S and O atomic neutrals - mainly by impact dissociation—and ions—mainly by electron impacts and by charge-exchange reactions (Bagenal & Dols, 2020). Due to the challenge of a continuous and simultaneous observation of the IPT, the neutral cloud and Io (both its atmosphere and its hot spots), there are still no definitive evidence on the mechanism driving the interplay between the variable volcanic activity observed on Io (e.g., de Kleer et al., 2019; de Pater et al., 2017), its atmosphere and the mass loading into the magnetosphere (Roth et al., 2020). More evidence are expected in the future, thanks to ground-based monitoring (Morgenthaler et al., 2022b) and from *Juno* dust observations (Jørgensen et al., 2020). As an external source, it was suggested that a global reconfiguration of the Jovian magnetosphere might drive injections of electrons from the middle and outer magnetosphere toward the inner magnetosphere (Louarn et al., 2014). These injections might affect the temperature and density of the IPT, and thus the local interaction at Io (Roth et al., 2020), ultimately determining the neutral supply and eventually the torus plasma loading—at least partially (Morgenthaler et al., 2022a). Unfortunately, no clear evidence or in-depth studies of this process are currently available. Given the complexity and the uncertainty on the above-mentioned processes, relying only on the footprint positions reported in this work to determine mass loading events appears overly ambitious. Nevertheless, the images shown in Figure 4 show evidence of variability in the plasma environment around Io. Therefore the auroral imaging of the IFP can help to reconstruct the timeline of the mass loading (or depletion) events that can occur in the IPT.

## 6. Conclusions

The present work represents the first attempt to constrain the plasma distribution along magnetic field lines crossing the Io Plasma Torus and its variability by analyzing the auroral footprints of Io in the Jovian ionosphere. This is possible thanks to the unique vantage point offered by the *Juno*'s polar orbit, together with the high spatial resolution of the JIRAM instrument. Deriving quantitative information on the plasma torus and its



variability from the Io footprint position can help complement ground-based and in situ observations that aim at understanding the complex interplay between Io, the Io Plasma Torus and the Jovian magnetosphere, especially regarding the changes in plasma supply within the torus. The variations of the properties of the Io Plasma Torus can be classified into four main types, namely: System III and System IV variations, local time asymmetry and temporal variations. In the present work, System III variations are not addressed by choosing images with similar longitudinal position of Io. In order to study the other types of variability, we determine the location of the auroral footprint by calculating the travel time for an alfvénic perturbation produced at Io to reach the Jovian ionospheres. The path traveled by the alfvénic perturbations and the position of the Io footprint depend on both the geometry and strength of the magnetic field and the plasma distribution along the field lines. Hence, we adopted a reverse approach: using the observed position of the Io footprint to determine the state of the Io Plasma Torus at different epochs. The Alfvén travel time is computed using the recent JRM33 magnetic field model based on *Juno*'s observations (Connerney et al., 2022) and a prescribed plasma density distribution along the field lines (Dougherty et al., 2017). After the sensitivity tests in Section 4.1, we describe the plasma distribution along the field lines with two main parameters, that is: the ion average temperature and the equatorial electron density. Although density and temperature are degenerate parameters in the present analysis (see Equation 8), the parameter spaces that best match the JIRAM observations shown in Figure 4 do not overlap (see Figure 3): this suggests the plasma environment around Io changes independent of the System III longitude.

We conclude:

1. We presented two sets of observations of the Io footprint, selected after inspecting the JIRAM database from PJ 1 to PJ 42 and covering nearly six years of observations. The selected data show variations in the position of the Io footprint related to intrinsic variation of the plasma conditions at the orbit of Io.
2. By analyzing the observations with Io at the same longitude in each set, we infer that the IPT state varies significantly between the epochs of each image. In particular, the IPT state variation was the largest between PJ 11 and PJ 32, when the electron density was  $<2,000 \text{ cm}^{-3}$  and  $2,750 \text{ cm}^{-3}$ , respectively (assuming the ion temperature from *Voyager 1*). Alternatively, the observations can be explained by an ion average temperature of 40 and 100 eV, respectively (assuming the same plasma density).
3. We tested different mixing ratio of  $\text{O}^+$ ,  $\text{S}^+$ ,  $\text{S}^{2+}$  and  $\text{S}^{3+}$  to investigate the sensitivity of the model, and we found that variations of these mixing ratios correlated with System IV variability have little effect on the position of the footprint. Therefore, it is unlikely that the variability detected in the JIRAM images was caused by the System IV periodicity.
4. We are not able to unequivocally determine if the variations of the Io footprint position are caused either by a local time asymmetry or by the temporal variability of the Io torus. Nevertheless, we can constrain the parameter space of the Io Plasma Torus by fitting the position of the Io footprint: this technique can thus be used to support the investigation on the interplay between Io, its torus and the magnetosphere.

## Data Availability Statement

JIRAM data and materials used in this study are publicly available on the Planetary Data System ([https://pds-atmospheres.nmsu.edu/data\\_and\\_services/atmospheres\\_data/JUNO/jiram.html](https://pds-atmospheres.nmsu.edu/data_and_services/atmospheres_data/JUNO/jiram.html), Adriani et al. (2019)).

Repository for the data products used in this study is: <https://doi.org/10.5281/zenodo.7496835> (Moirano, 2023).

## References

- Acuña, M. H., Neubauer, F. M., & Ness, N. F. (1981). Standing Alfvén wave current system at Io: Voyager 1 observations. *Journal of Geophysical Research*, 86(A10), 8513–8521. <https://doi.org/10.1029/JA086iA10p08513>
- Adriani, A., Filacchione, G., Di Iorio, T., Turrini, D., Noschese, R., Cicchetti, A., et al. (2017). JIRAM, the Jovian infrared auroral mapper. *Space Science Reviews*, 213(1–4), 393–446. <https://doi.org/10.1007/s11214-014-0094-y>
- Adriani, A., Mura, A., Orton, G., Hansen, C., Altieri, F., Moriconi, M. L., et al. (2018). Clusters of cyclones encircling Jupiter's poles. *Nature*, 555(7695), 216–219. <https://doi.org/10.1038/nature25491>
- Adriani, A., Noschese, R., & Huber, L. (2019). Juno JIRAM bundle. [Dataset]. PDS Atmospheres (ATM). <https://doi.org/10.17189/1518967>
- Bagenal, F. (1994). Empirical model of the Io plasma torus: Voyager measurements. *Journal of Geophysical Research*, 99(A6), 11043. <https://doi.org/10.1029/93JA02908>
- Bagenal, F., Adriani, A., Allegrini, F., Bolton, S. J., Bonfond, B., Bunce, E. J., et al. (2017). Magnetospheric science objectives of the Juno mission. *Space Science Reviews*, 213(1–4), 219–287. <https://doi.org/10.1007/s11214-014-0036-8>
- Bagenal, F., Crary, F. J., Stewart, A. I. F., Schneider, N. M., Gurnett, D. A., Kurth, W. S., et al. (1997). Galileo measurements of plasma density in the Io torus. *Geophysical Research Letters*, 24(17), 2119–2122. <https://doi.org/10.1029/97GL01254>

## Acknowledgments

The authors thank Agenzia Spaziale Italiana (ASI) for supporting the JIRAM contribution to the Juno mission (including this work) under the ASI contract 2016-23-H.0. This work was also funded by the NASA New Frontiers Program for Juno (managed by the Jet Propulsion Laboratory) via a subcontract with Southwest Research Institute. We are grateful to NASA and contributing institutions that have made the Juno mission possible. B. Bonfond, D. Grodent, and J.-C. Gérard are funded by the Belgian Federal Science Policy Office (BELSPO) via the PRODEX Program of European Space Agency (ESA). V. Dols acknowledges the support of the NASA Solar System Workings Grant 80NSSC22K0109.

- Bagenal, F., & Dols, V. (2020). The space environment of Io and Europa. *Journal of Geophysical Research: Space Physics*, 125(5). <https://doi.org/10.1029/2019JA027485>
- Bagenal, F., & Sullivan, J. D. (1981). Direct plasma measurements in the Io torus and inner magnetosphere of Jupiter. *Journal of Geophysical Research*, 86(A10), 8447–8466. <https://doi.org/10.1029/JA086iA10p08447>
- Barbosa, D. D., & Kiverson, M. G. (1983). Dawn-dusk electric field asymmetry of the Io plasma torus. *Geophysical Research Letters*, 10(3), 210–213. <https://doi.org/10.1029/GL010i003p00210>
- Belcher, J. W., Goertz, C. K., Sullivan, J. D., & Acuña, M. H. (1981). Plasma observations of the Alfvén wave generated by Io. *Journal of Geophysical Research*, 86(A10), 8508–8512. <https://doi.org/10.1029/JA086iA10p08508>
- Bertotti, B., Comoretto, G., & Iess, L. (1993). Doppler tracking of spacecraft with multi-frequency links. *Astronomy & Astrophysics*, 269(1–2), 608–616.
- Bhattacharyya, D., Clarke, J. T., Montgomery, J., Bonfond, B., Gérard, J., & Grodent, D. (2018). Evidence for auroral emissions from Callisto's footprint in HST UV images. *Journal of Geophysical Research: Space Physics*, 123(1), 364–373. <https://doi.org/10.1002/2017JA024791>
- Bird, M., Asmar, S., Edenhofer, P., Funke, O., Pätzold, M., & Volland, H. (1993). The structure of Jupiter's Io plasma torus inferred from Ulysses radio occultation observations. *Planetary and Space Science*, 41(11–12), 999–1010. [https://doi.org/10.1016/0032-0633\(93\)90104-A](https://doi.org/10.1016/0032-0633(93)90104-A)
- Bodisch, K. M., Dougherty, L. P., & Bagenal, F. (2017). Survey of Voyager plasma science ions at Jupiter: 3. Protons and minor ions. *Journal of Geophysical Research: Space Physics*, 122(8), 8277–8294. <https://doi.org/10.1002/2017JA024148>
- Bolton, S. J., Lunine, J., Stevenson, D., Connerney, J. E. P., Levin, S., Owen, T. C., et al. (2017). The Juno mission. *Space Science Reviews*, 213(1), 5–37. <https://doi.org/10.1007/s11214-017-0429-6>
- Bonfond, B. (2012). When moons create aurora: The satellite footprints on giant planets. In *Auroral phenomenology and magnetospheric processes: Earth and other planets* (pp. 133–140). American Geophysical Union (AGU). <https://doi.org/10.1029/2011GM001169>
- Bonfond, B., Grodent, D., Badman, S. V., Saur, J., Gérard, J. C., & Radioti, A. (2017). Similarity of the Jovian satellite footprints: Spots multiplicity and dynamics. *Icarus*, 292, 208–217. <https://doi.org/10.1016/j.icarus.2017.01.009>
- Bonfond, B., Grodent, D., Gérard, J.-C., Radioti, A., Saur, J., & Jacobsen, S. (2008). UV Io footprint leading spot: A key feature for understanding the UV Io footprint multiplicity? *Geophysical Research Letters*, 35(5), L05107. <https://doi.org/10.1029/2007GL032418>
- Bonfond, B., Hess, S., Bagenal, F., Gérard, J.-C., Grodent, D., Radioti, A., et al. (2013). The multiple spots of the Ganymede auroral footprint. *Geophysical Research Letters*, 40(19), 4977–4981. <https://doi.org/10.1002/grl.50989>
- Bonfond, B., Hess, S., Gérard, J. C., Grodent, D., Radioti, A., Chantry, V., et al. (2013). Evolution of the Io footprint brightness I: Far-UV observations. *Planetary and Space Science*, 88, 64–75. <https://doi.org/10.1016/j.pss.2013.05.023>
- Bonfond, B., Saur, J., Grodent, D., Badman, S. V., Bisikalo, D., Shemansky, V., et al. (2017). The tails of the satellite auroral footprints at Jupiter. *Journal of Geophysical Research: Space Physics*, 122(8), 7985–7996. <https://doi.org/10.1002/2017JA024370>
- Bonfond, B., Yao, Z. H., Gladstone, G. R., Grodent, D., Gérard, J.-C., Matar, J., et al. (2021). Are dawn storms Jupiter's auroral substorms? *AGU Advances*, 2(1), e2020AV000275. <https://doi.org/10.1029/2020AV000275>
- Broadfoot, A. L., Belton, M. J. S., Takacs, P. Z., Sandel, B. R., Shemansky, D. E., Holberg, J. B., et al. (1979). June). Extreme ultraviolet observations from Voyager 1 encounter with Jupiter. *Science*, 204(4396), 979–982. <https://doi.org/10.1126/science.204.4396.979>
- Brown, M. E. (1995). Periodicities in the Io plasma torus. *Journal of Geophysical Research*, 100(A11), 21683–21695. <https://doi.org/10.1029/95JA01988>
- Brown, M. E., & Bouchez, A. H. (1997). The response of Jupiter's magnetosphere to an outburst on Io. *Science*, 278(5336), 268–271. <https://doi.org/10.1126/science.278.5336.268>
- Caldwell, J., Turgeon, B., & Hua, X.-M. (1992). Hubble space telescope imaging of the North polar aurora on Jupiter. *Science*, 257(5076), 1512–1515. <https://doi.org/10.1126/science.257.5076.1512>
- Chenette, D. L., Conlon, T. F., & Simpson, J. A. (1974). Bursts of relativistic electrons from Jupiter observed in interplanetary space with the time variation of the planetary rotation period. *Journal of Geophysical Research (1896-1977)*, 79(25), 3551–3558. <https://doi.org/10.1029/JA079i025p03551>
- Clark, R. N., & Mc Cord, T. B. (1980). The Galilean satellites: New near-infrared spectral reflectance measurements (0.65–2.5  $\mu\text{m}$ ) and a 0.325–5  $\mu\text{m}$  summary. *Icarus*, 41(3), 323–339. [https://doi.org/10.1016/0019-1035\(80\)90217-1](https://doi.org/10.1016/0019-1035(80)90217-1)
- Clarke, J. T., Ajello, J., Ballester, G., Ben Jaffel, L., Connerney, J., Gérard, J.-C., et al. (2002). Ultraviolet emissions from the magnetic footprints of Io, Ganymede and Europa on Jupiter. *Nature*, 415(6875), 997–1000. <https://doi.org/10.1038/415997a>
- Clarke, J. T., Ballester, G. E., Trauger, J., Evans, R., Connerney, J. E. P., Stapelfeldt, K., et al. (1996). Far-ultraviolet imaging of Jupiter's aurora and the Io "footprint". *Science*, 274(5286), 404–409. <https://doi.org/10.1126/science.274.5286.404>
- Connerney, J. E. P., Baron, R., Satoh, T., & Owen, T. (1993). Images of excited  $\text{H}_3^+$  at the foot of the Io flux tube in Jupiter's atmosphere. *Science*, 262(5136), 1035–1038. <https://doi.org/10.1126/science.262.5136.1035>
- Connerney, J. E. P., Timmins, S., Herceg, M., & Joergensen, J. L. (2020). A Jovian magnetodisc model for the Juno era. *Journal of Geophysical Research: Space Physics*, 125(10), e2020JA028138. <https://doi.org/10.1029/2020JA028138>
- Connerney, J. E. P., Timmins, S., Oliverson, R. J., Espley, J. R., Joergensen, J. L., Kotsiaros, S., et al. (2022). A new model of Jupiter's magnetic field at the completion of Juno's prime mission. *Journal of Geophysical Research: Planets*, 127(2), e2021JE007055. <https://doi.org/10.1029/2021JE007055>
- Copper, M., Delamere, P. A., & Overcast-Howe, K. (2016). Modeling physical chemistry of the Io plasma torus in two dimensions. *Journal of Geophysical Research: Space Physics*, 121(7), 6602–6619. <https://doi.org/10.1002/2016JA022767>
- Crary, F. J., Bagenal, F., Ansher, J. A., Gurnett, D. A., & Kurth, W. S. (1996). Anisotropy and proton density in the Io plasma torus derived from whistler wave dispersion. *Journal of Geophysical Research*, 101(A2), 2699–2706. <https://doi.org/10.1029/95JA02212>
- Crary, F. J., Bagenal, F., Frank, L. A., & Paterson, W. R. (1998). Galileo plasma spectrometer measurements of composition and temperature in the Io plasma torus. *Journal of Geophysical Research*, 103(A12), 29359–29370. <https://doi.org/10.1029/1998JA090003>
- Damiano, P. A., Delamere, P. A., Stauffer, B., Ng, C.-S., & Johnson, J. R. (2019). Kinetic simulations of electron acceleration by dispersive scale Alfvén waves in Jupiter's magnetosphere. *Geophysical Research Letters*, 46(6), 3043–3051. <https://doi.org/10.1029/2018GL081219>
- Davies, A. G. (2001). Volcanism on Io: The view from Galileo. *Astronomy and Geophysics*, 42(2), 2.10–2.16. <https://doi.org/10.1046/j.1468-4004.2001.42210.x>
- de Kleer, K., Nimmo, F., & Kite, E. (2019). Variability in Io's volcanism on timescales of periodic orbital changes. *Geophysical Research Letters*, 46(12), 6327–6332. <https://doi.org/10.1029/2019GL082691>
- Delamere, P. A., & Bagenal, F. (2003). Modeling variability of plasma conditions in the Io torus. *Journal of Geophysical Research*, 108(A7), 1276. <https://doi.org/10.1029/2002JA009706>
- Delamere, P. A., Bagenal, F., & Steffl, A. (2005). Radial variations in the Io plasma torus during the Cassini era. *Journal of Geophysical Research*, 110(A12), A12223. <https://doi.org/10.1029/2005JA011251>

- Delamere, P. A., Steffl, A., & Bagenal, F. (2004). Modeling temporal variability of plasma conditions in the Io torus during the Cassini era. *Journal of Geophysical Research*, *109*(A10), A10216. <https://doi.org/10.1029/2003JA010354>
- de Pater, I., de Kleer, K., Davies, A. G., & Ádámkóvics, M. (2017). Three decades of Loki Patera observations. *Icarus*, *297*, 265–281. <https://doi.org/10.1016/j.icarus.2017.03.016>
- Dols, V., Gérard, J. C., Paresse, F., Prangé, R., & Vidal-Madjar, A. (1992). Ultraviolet imaging of the Jovian aurora with the Hubble space telescope. *Geophysical Research Letters*, *19*(18), 1803–1806. <https://doi.org/10.1029/92GL02104>
- Dougherty, L. P., Bodisch, K. M., & Bagenal, F. (2017). Survey of voyager plasma science ions at Jupiter: 2. Heavy ions. *Journal of Geophysical Research: Space Physics*, *122*(8), 8257–8276. <https://doi.org/10.1002/2017JA024053>
- Drell, S. D., Foley, H. M., & Ruderman, M. A. (1965). Drag and propulsion of large satellites in the ionosphere; An Alfvén propulsion engine in space. *Physical Review Letters*, *14*(6), 171–175. <https://doi.org/10.1103/PhysRevLett.14.171>
- Drossart, P., Maillard, J., Caldwell, J., Kim, S., Watson, J., Majewski, W., et al. (1989). Detection of H<sub>3</sub><sup>+</sup> on Jupiter. *Nature*, *340*(6234), 539–541. <https://doi.org/10.1038/340539a0>
- Dunn, W. R., Gray, R., Wibisono, A. D., Lamy, L., Louis, C., Badman, S. V., et al. (2020). Comparisons between Jupiter's X-ray, UV and radio emissions and in-situ solar wind measurements during 2007. *Journal of Geophysical Research: Space Physics*, *125*(6), e2019JA027222. <https://doi.org/10.1029/2019JA027222>
- Gérard, J.-C., Mura, A., Bonfond, B., Gladstone, G., Adriani, A., Hue, V., et al. (2018). Concurrent ultraviolet and infrared observations of the North Jovian aurora during Juno's first Perijove. *Icarus*, *312*, 145–156. <https://doi.org/10.1016/j.icarus.2018.04.020>
- Gérard, J.-C., Saglam, A., Grodent, D., & Clarke, J. T. (2006). Morphology of the ultraviolet Io footprint emission and its control by Io's location. *Journal of Geophysical Research*, *111*(A4), A04202. <https://doi.org/10.1029/2005JA011327>
- Gladstone, G. R., Stern, S. A., Slater, D. C., Versteeg, M., Davis, M. W., Retherford, K. D., et al. (2007). Jupiter's nightside airglow and aurora. *Science*, *318*(5848), 229–231. <https://doi.org/10.1126/science.1147613>
- Gladstone, G. R., Waite, J. H., Grodent, D., Lewis, W. S., Cray, F. J., Elsner, R. F., et al. (2002). A pulsating auroral X-ray hot spot on Jupiter. *Nature*, *415*(6875), 1000–1003. <https://doi.org/10.1038/4151000a>
- Grodent, D. (2015). A brief review of ultraviolet auroral emissions on giant planets. *Space Science Reviews*, *187*(1–4), 23–50. <https://doi.org/10.1007/s11214-014-0052-8>
- Grodent, D., Gérard, J.-C., Gustin, J., Mauk, B. H., Connerney, J. E. P., & Clarke, J. T. (2006). Europa's FUV auroral tail on Jupiter. *Geophysical Research Letters*, *33*(6), L06201. <https://doi.org/10.1029/2005GL025487>
- Grodent, D., Waite, J. H., Jr., & Gérard, J.-C. (2001). A self-consistent model of the Jovian auroral thermal structure. *Journal of Geophysical Research*, *106*(A7), 12933–12952. <https://doi.org/10.1029/2000JA900129>
- Herbert, F., Schneider, N. M., & Dessler, A. J. (2008). New description of Io's cold plasma torus. *Journal of Geophysical Research*, *113*(A1). <https://doi.org/10.1029/2007JA012555>
- Hess, S. L. G., Bonfond, B., Chantry, V., Gérard, J. C., Grodent, D., Jacobsen, S., & Radioti, A. (2013). Evolution of the Io footprint brightness II: Modeling. *Planetary and Space Science*, *88*, 76–85. <https://doi.org/10.1016/j.pss.2013.08.005>
- Hess, S. L. G., Delamere, P., Dols, V., Bonfond, B., & Swift, D. (2010). Power transmission and particle acceleration along the Io flux tube. *Journal of Geophysical Research*, *115*(A6). <https://doi.org/10.1029/2009JA014928>
- Hess, S. L. G., Delamere, P. A., Bagenal, F., Schneider, N., & Steffl, A. J. (2011). Longitudinal modulation of hot electrons in the Io plasma torus. *Journal of Geophysical Research*, *116*(A11). <https://doi.org/10.1029/2011JA016918>
- Hikida, R., Yoshioka, K., Tsuchiya, F., Kagitani, M., Kimura, T., Bagenal, F., et al. (2020). Spatially asymmetric increase in hot electron fraction in the Io plasma torus during volcanically active period revealed by observations by Hisaki/EXCEED from November 2014 to May 2015. *Journal of Geophysical Research: Space Physics*, *125*(3), e2019JA027100. <https://doi.org/10.1029/2019JA027100>
- Hill, T. W., Dessler, A. J., & Michel, F. C. (1974). Configuration of the Jovian magnetosphere. *Geophysical Research Letters*, *1*(1), 3–6. <https://doi.org/10.1029/GL001i001p00003>
- Hinton, P. C., Bagenal, F., & Bonfond, B. (2019). Alfvén wave propagation in the Io plasma torus. *Geophysical Research Letters*, *46*(3), 1242–1249. <https://doi.org/10.1029/2018GL081472>
- Huscher, E., Bagenal, F., Wilson, R. J., Allegrini, F., Ebert, R. W., Valek, P. W., et al. (2021). Survey of Juno observations in Jupiter's plasma disk: Density. *Journal of Geophysical Research: Space Physics*, *126*(8), e2021JA029446. <https://doi.org/10.1029/2021JA029446>
- Ingersoll, A. P., Vasavada, A. R., Little, B., Anger, C. D., Bolton, S. J., Alexander, C., et al. (1998). Imaging Jupiter's aurora at visible wavelengths. *Icarus*, *135*(1), 251–264. <https://doi.org/10.1006/icar.1998.5971>
- Ip, W.-H., & Goertz, C. K. (1983). An interpretation of the dawn–dusk asymmetry of UV emission from the Io plasma torus. *Nature*, *302*(5905), 232–233. <https://doi.org/10.1038/302232a0>
- Jacobsen, S., Neubauer, F. M., Saur, J., & Schilling, N. (2007). Io's nonlinear MHD-wave field in the heterogeneous Jovian magnetosphere. *Geophysical Research Letters*, *34*(10), L10202. <https://doi.org/10.1029/2006GL029187>
- Jacobsen, S., Saur, J., Neubauer, F. M., Bonfond, B., Gérard, J.-C., & Grodent, D. (2010). Location and spatial shape of electron beams in Io's wake. *Journal of Geophysical Research*, *115*(A4). <https://doi.org/10.1029/2009JA014753>
- Jones, S. T., & Su, Y.-J. (2008). Role of dispersive Alfvén waves in generating parallel electric fields along the Io–Jupiter fluxtube. *Journal of Geophysical Research*, *113*(A12). <https://doi.org/10.1029/2008JA013512>
- Jørgensen, J. L., Denver, T., Benn, M., Jørgensen, P. S., Hecceg, M., Merayo, J. M. G., & Connerney, J. E. P. (2020). A profile of the Io dust cloud and plasma torus as observed from Juno (Technical report no. EGU2020-18093). Copernicus meetings. <https://doi.org/10.5194/egusphere-egu2020-18093>
- Kaiser, M. L., & Desch, M. D. (1980). Narrow-band Jovian kilometric radiation: A new radio component. *Geophysical Research Letters*, *7*(5), 389–392. <https://doi.org/10.1029/GL007i005p00389>
- Kennel, C. F., & Coroniti, F. V. (1977). Possible origins of time variability in Jupiter's outer magnetosphere, 2. Variations in solar wind magnetic field. *Geophysical Research Letters*, *4*(6), 215–218. <https://doi.org/10.1029/GL004i006p00215>
- Kivelson, M. G., Bagenal, F., Kurth, W. S., Neubauer, F. M., Paranicas, C., & Saur, J. (2004). Magnetospheric interactions with satellites. In F. Bagenal (Ed.), *Jupiter: The planet, satellites and magnetosphere* (Vol. 21, p. 513). Cambridge University Press.
- Koga, R., Tsuchiya, F., Kagitani, M., Sakanoi, T., Yoshioka, K., Yoshikawa, I., et al. (2019). Transient change of Io's neutral oxygen cloud and plasma torus observed by Hisaki. *Journal of Geophysical Research: Space Physics*, *124*(12), 10318–10331. <https://doi.org/10.1029/2019JA026877>
- Kupo, I., Mekler, Y., & Eviatar, A. (1976). Detection of ionized sulfur in the Jovian magnetosphere. *Astrophysical Journal*, *205*, L51. <https://doi.org/10.1086/182088>
- Kurth, W. S., Imai, M., Hospodarsky, G. B., Gurnett, D. A., Louarn, P., Valek, P., et al. (2017). A new view of Jupiter's auroral radio spectrum. *Geophysical Research Letters*, *44*(14), 7114–7121. <https://doi.org/10.1002/2017GL072889>

- Lichtenberg, G., Thomas, N., & Fouchet, T. (2001). Detection of S (IV) 10.51  $\mu\text{m}$  emission from the Io plasma torus. *Journal of Geophysical Research*, *106*(A12), 29899–29910. <https://doi.org/10.1029/2001JA900020>
- Livengood, T. A., Moos, H. W., Ballester, G. E., & Prangé, R. M. (1992). Jovian ultraviolet auroral activity, 1981–1991. *Icarus*, *97*(1), 26–45. [https://doi.org/10.1016/0019-1035\(92\)90055-C](https://doi.org/10.1016/0019-1035(92)90055-C)
- Lopes, R. M., & Williams, D. A. (2015). Volcanism on Io. In *The encyclopedia of volcanoes* (pp. 747–762). Elsevier. <https://doi.org/10.1016/B978-0-12-385938-9.00043-2>
- Louarn, P., Paranicas, C. P., & Kurth, W. S. (2014). Global magnetodisk disturbances and energetic particle injections at Jupiter. *Journal of Geophysical Research: Space Physics*, *119*(6), 4495–4511. <https://doi.org/10.1002/2014JA019846>
- Lysak, R. L., & Song, Y. (2003). Kinetic theory of the Alfvén wave acceleration of auroral electrons. *Journal of Geophysical Research*, *108*(A4), 8005. <https://doi.org/10.1029/2002JA009406>
- Lysak, R. L., Song, Y., Elliott, S., Kurth, W., Sulaiman, A. H., & Gershman, D. (2021). The Jovian ionospheric Alfvén resonator and auroral particle acceleration. *Journal of Geophysical Research: Space Physics*, *126*(12), e2021JA029886. <https://doi.org/10.1029/2021JA029886>
- McComas, D. J., Alexander, N., Allegrini, F., Bagenal, F., Beebe, C., Clark, G., et al. (2017). The Jovian Auroral Distributions Experiment (JADE) on the Juno mission to Jupiter. *Space Science Reviews*, *213*(1), 547–643. <https://doi.org/10.1007/s11214-013-9990-9>
- McDonnell, W. J., Goldstein, D. B., Varghese, P. L., & Trafton, L. M. (2019). Simulation of Io's plumes and Jupiter's plasma torus. *Physics of Fluids*, *31*(7), 077103. <https://doi.org/10.1063/1.5097961>
- Mei, Y., Thorne, R. M., & Bagenal, F. (1995). Analytical model for the density distribution in the Io plasma torus. *Journal of Geophysical Research*, *100*(A2), 1823–1828. <https://doi.org/10.1029/94JA02359>
- Miller, S., Tennyson, J., Geballe, T. R., & Stallard, T. (2020). Thirty years of H<sub>3</sub><sup>+</sup> astronomy. *Reviews of Modern Physics*, *92*(3), 035003. <https://doi.org/10.1103/RevModPhys.92.035003>
- Moirano, A. (2023). Variability of the auroral footprint of Io detected by Juno-JIRAM and modelling of the Io plasma torus. [Dataset]. Zenodo. <https://doi.org/10.5281/zenodo.7496835>
- Moirano, A., Gomez Casajus, L., Zannoni, M., Durante, D., & Tortora, P. (2021). Morphology of the Io plasma torus from Juno radio occultations. *Journal of Geophysical Research: Space Physics*, *126*(10), e2021JA029190. <https://doi.org/10.1029/2021JA029190>
- Moirano, A., Mura, A., Adriani, A., Dols, V., Bonfond, B., Waite, J. H., et al. (2021). Morphology of the auroral tail of Io, Europa, and Ganymede from JIRAM L-band imager. *Journal of Geophysical Research: Space Physics*, *126*(9), e2021JA029450. <https://doi.org/10.1029/2021JA029450>
- Morgan, J. S. (1985). Temporal and spatial variations in the Io torus. *Icarus*, *62*(3), 389–414. [https://doi.org/10.1016/0019-1035\(85\)90183-6](https://doi.org/10.1016/0019-1035(85)90183-6)
- Morgenthaler, J. P., Schmidt, C., Marconi, M., Vogt, M., & Schneider, N. (2022a). Using Io Input/Output observatory (IoIO) observations to determine if mass flow in Jupiter's magnetosphere driven by internal or external processes. Paper presented at Magnetosphere of the Outer Planets Meeting 2022, Liege, Belgium.
- Morgenthaler, J. P., Schmidt, C., Marconi, M., Vogt, M. F., & Schneider, N. M. (2022b). Find your favorite Io volcanic enhancement! A global view of the Jovian magnetosphere during the Juno mission as recorded by PSI's Io input/output observatory (IoIO). AGU Fall Meeting 2022.
- Mura, A., Adriani, A., Altieri, F., Connerney, J. E. P., Bolton, S. J., Moriconi, M. L., et al. (2017). Infrared observations of Jovian aurora from Juno's first orbits: Main oval and satellite footprints: Jovian Aurora IR Observations from Juno. *Geophysical Research Letters*, *44*(11), 5308–5316. <https://doi.org/10.1002/2017GL072954>
- Mura, A., Adriani, A., Connerney, J. E. P., Bolton, S., Altieri, F., Bagenal, F., et al. (2018). Juno observations of spot structures and a split tail in Io-induced aurora on Jupiter. *Science*, *361*(6404), 774–777. <https://doi.org/10.1126/science.aat1450>
- Murakami, G., Yoshioka, K., Yamazaki, A., Tsuchiya, F., Kimura, T., Tao, C., et al. (2016). Response of Jupiter's inner magnetosphere to the solar wind derived from extreme ultraviolet monitoring of the Io plasma torus. *Geophysical Research Letters*, *43*(24), 12308–12316. <https://doi.org/10.1002/2016GL071675>
- Nerney, E. G., & Bagenal, F. (2020). Combining UV spectra and physical chemistry to constrain the hot electron fraction in the Io plasma torus. *Journal of Geophysical Research: Space Physics*, *125*(4), e2019JA027458. <https://doi.org/10.1029/2019JA027458>
- Neubauer, F. (1980). Nonlinear standing Alfvén wave current system at Io: Theory. *Journal of Geophysical Research*, *85*(A3), 1171–1178. <https://doi.org/10.1029/JA085iA03p01171>
- Nichols, J. D., Allegrini, F., Bagenal, F., Bunce, E. J., Cowley, S. W. H., Ebert, R. W., et al. (2020). An enhancement of Jupiter's main auroral emission and magnetospheric currents. *Journal of Geophysical Research: Space Physics*, *125*(8), e2020JA027904. <https://doi.org/10.1029/2020JA027904>
- Oka, T. (1980). Observation of the infrared spectrum of H<sub>3</sub><sup>+</sup>. *Physical Review Letters*, *45*(7), 531–534. <https://doi.org/10.1103/PhysRevLett.45.531>
- Phipps, P. H., Withers, P., Buccino, D. R., Yang, Y.-M., & Parisi, M. (2021). Two years of observations of the Io plasma torus by Juno radio occultations: Results from perijoves 1 to 15. *Journal of Geophysical Research: Space Physics*, *126*(3), e2020JA028710. <https://doi.org/10.1029/2020JA028710>
- Phipps, P. H., Withers, P., Vogt, M. F., Buccino, D. R., Yang, Y., Parisi, M., et al. (2020). Where is the Io plasma torus? A comparison of observations by Juno radio occultations to predictions from Jovian magnetic field models. *Journal of Geophysical Research: Space Physics*, *125*(8), <https://doi.org/10.1029/2019JA027633>
- Prangé, R., Rego, D., Southwood, D., Zarka, P., Miller, S., & Ip, W. (1996). Rapid energy dissipation and variability of the Io–Jupiter electrodynamic circuit. *Nature*, *379*(6563), 323–325. <https://doi.org/10.1038/379323a0>
- Roesler, F. L., Scherb, F., & Oliverson, R. J. (1984). Periodic intensity variation in [SIII] 9531 Å emission from the Jupiter plasma torus. *Geophysical Research Letters*, *11*(2), 128–130. <https://doi.org/10.1029/GL011i002p00128>
- Roth, L., Boissier, J., Moullet, A., Sánchez-Monge, A., de Kleer, K., Yoneda, M., et al. (2020). An attempt to detect transient changes in Io's SO<sub>2</sub> and NaCl atmosphere. *Icarus*, *350*, 113925. <https://doi.org/10.1016/j.icarus.2020.113925>
- Sandel, B. R., & Broadfoot, A. L. (1982a). Discovery of an Io-correlated energy source for Io's hot plasma torus. *Journal of Geophysical Research*, *87*(A4), 2231–2240. <https://doi.org/10.1029/JA087iA04p02231>
- Sandel, B. R., & Broadfoot, A. L. (1982b). Io's hot plasma torus—A synoptic view from Voyager. *Journal of Geophysical Research*, *87*(A1), 212–218. <https://doi.org/10.1029/JA087iA01p00212>
- Sandel, B. R., & Dessler, A. J. (1988). Dual periodicity of the Jovian magnetosphere. *Journal of Geophysical Research*, *93*(A6), 5487–5504. <https://doi.org/10.1029/JA093iA06p05487>
- Sandel, B. R., Shemansky, D. E., Broadfoot, A. L., Bertaux, J. L., Blamont, J. E., Belton, M. J. S., et al. (1979). Extreme ultraviolet observations from Voyager 2 encounter with Jupiter. *Science*, *206*(4421), 962–966. <https://doi.org/10.1126/science.206.4421.962>
- Saur, J. (2004). A model of Io's local electric field for a combined Alfvénic and unipolar inductor far-field coupling. *Journal of Geophysical Research*, *109*(A1), A01210. <https://doi.org/10.1029/2002JA009354>
- Schlegel, S., & Saur, J. (2022). Alternating emission features in Io's footprint tail: Magnetohydrodynamical simulations of possible causes. *Journal of Geophysical Research: Space Physics*, *127*(5), e2021JA030243. <https://doi.org/10.1029/2021JA030243>

- Schmidt, C., Schneider, N., Leblanc, F., Gray, C., Morgenthaler, J., Turner, J., & Grava, C. (2018). A survey of visible S+ emission in Io's plasma torus during the Hisaki epoch. *Journal of Geophysical Research: Space Physics*, *123*(7), 5610–5624. <https://doi.org/10.1029/2018JA025296>
- Schneider, N. M., & Trauger, J. T. (1995). The structure of the Io torus. *Astrophysical Journal*, *450*, 450. <https://doi.org/10.1086/176155>
- Skinner, T. E., Durrance, S. T., Feldman, P. D., & Moos, H. W. (1984). IUE observations of longitudinal and temporal variations in the Jovian auroral emission. *The Astrophysical Journal*, *278*, 441–448. <https://doi.org/10.1086/161809>
- Smyth, W. H., Peterson, C. A., & Marconi, M. L. (2011). A consistent understanding of the ribbon structure for the Io plasma torus at the Voyager 1, 1991 ground-based, and Galileo J0 epochs. *Journal of Geophysical Research*, *116*(A7). <https://doi.org/10.1029/2010JA016094>
- Steffl, A., Delamere, P., & Bagenal, F. (2006). Cassini UVIS observations of the Io plasma torus III. Observations of temporal and azimuthal variability. *Icarus*, *180*(1), 124–140. <https://doi.org/10.1016/j.icarus.2005.07.013>
- Steffl, A., Delamere, P., & Bagenal, F. (2008). Cassini UVIS observations of the Io plasma torus. *Icarus*, *194*(1), 153–165. <https://doi.org/10.1016/j.icarus.2007.09.019>
- Sulaiman, A. H., Hospodarsky, G. B., Elliott, S. S., Kurth, W. S., Gurnett, D. A., Imai, M., et al. (2020). Wave-particle interactions associated with Io's auroral footprint: Evidence of Alfvén, ion cyclotron, and whistler modes. *Geophysical Research Letters*, *47*(22). <https://doi.org/10.1029/2020GL088432>
- Szalay, J. R., Allegrini, F., Bagenal, F., Bolton, S. J., Bonfond, B., Clark, G., et al. (2020). A new framework to explain changes in Io's footprint tail electron fluxes. *Geophysical Research Letters*, *47*(18). <https://doi.org/10.1029/2020GL089267>
- Tao, C., Badman, S. V., & Fujimoto, M. (2011). UV and IR auroral emission model for the outer planets: Jupiter and Saturn comparison. *Icarus*, *213*(2), 581–592. <https://doi.org/10.1016/j.icarus.2011.04.001>
- Thomas, N. (1992). Optical observations of Io's neutral clouds and plasma torus. *Surveys in Geophysics*, *13*(2), 91–164. <https://doi.org/10.1007/BF01903525>
- Thomas, N. (1995). Ion temperatures in the Io plasma torus. *Journal of Geophysical Research*, *100*(A5), 7925–7935. <https://doi.org/10.1029/94JA03143>
- Thomas, N., Bagenal, F., Hill, T. W., & Wilson, J. K. (2004). The Io neutral clouds and plasma torus. In F. Bagenal, T. E. Dowling, & W. B. McKinnon (Eds.), *Jupiter. The planet, satellites and magnetosphere* (Vol. 1, pp. 561–591).
- Thomas, N., & Lichtenberg, G. (1997). The latitudinal dependence of ion temperature in the Io plasma torus. *Geophysical Research Letters*, *24*(10), 1175–1178. <https://doi.org/10.1029/97GL01133>
- Trafton, L., Carr, J., Lester, D., & Harvey, P. (1989). *Jupiter's aurora: Detection of quadrupole h2 emission* (p. 494). NASA Special Publication.
- Tsuchiya, F., Arakawa, R., Misawa, H., Kagitani, M., Koga, R., Suzuki, F., et al. (2019). Azimuthal variation in the Io plasma torus observed by the Hisaki satellite from 2013 to 2016. *Journal of Geophysical Research: Space Physics*, *124*(5), 3236–3254. <https://doi.org/10.1029/2018JA026038>
- Tsuchiya, F., Yoshioka, K., Kimura, T., Koga, R., Murakami, G., Yamazaki, A., et al. (2018). Enhancement of the Jovian magnetospheric plasma Circulation caused by the change in plasma supply from the satellite Io. *Journal of Geophysical Research: Space Physics*, *123*(8), 6514–6532. <https://doi.org/10.1029/2018JA025316>
- Vasavada, A. R., Bouchez, A. H., Ingersoll, A. P., Little, B., & Anger, C. D. (1999). Jupiter's visible aurora and Io footprint. *Journal of Geophysical Research*, *104*(E11), 27133–27142. <https://doi.org/10.1029/1999JE001055>
- Vogt, M. F., Connerney, J. E., DiBraccio, G. A., Wilson, R. J., Thomsen, M. F., Ebert, R. W., et al. (2020). Magnetotail reconnection at Jupiter: A survey of Juno magnetic field observations. *Journal of Geophysical Research: Space Physics*, *125*(3), e2019JA027486. <https://doi.org/10.1029/2019JA027486>
- Wu, W., Peng, S., Ma, T., Ren, H., Zhang, J., Zhang, T., et al. (2019). Status of high current H2+ and H3+ ion sources. *Review of Scientific Instruments*, *90*(10), 101501. <https://doi.org/10.1063/1.5109240>
- Yao, Z. H., Bonfond, B., Grodent, D., Chané, E., Dunn, W. R., Kurth, W. S., et al. (2022). On the relation between auroral morphologies and compression conditions of Jupiter's magnetopause: Observations from Juno and the Hubble space telescope. *Journal of Geophysical Research: Space Physics*, *127*(10), e2021JA029894. <https://doi.org/10.1029/2021JA029894>
- Yao, Z. H., Dunn, W. R., Woodfield, E. E., Clark, G., Mauk, B. H., Ebert, R. W., et al. (2021). Revealing the source of Jupiter's x-ray auroral flares. *Science Advances*, *7*(28), eabf0851. <https://doi.org/10.1126/sciadv.abf0851>
- Yoneda, M., Nozawa, H., Misawa, H., Kagitani, M., & Okano, S. (2010). Jupiter's magnetospheric change by Io's volcanoes. *Geophysical Research Letters*, *37*(11). <https://doi.org/10.1029/2010GL043656>
- Yoneda, M., Tsuchiya, F., Misawa, H., Bonfond, B., Tao, C., Kagitani, M., & Okano, S. (2013). Io's volcanism controls Jupiter's radio emissions. *Geophysical Research Letters*, *40*(4), 671–675. <https://doi.org/10.1002/grl.50095>
- Yoshioka, K., Tsuchiya, F., Kagitani, M., Kimura, T., Murakami, G., Fukuyama, D., et al. (2018). The influence of Io's 2015 volcanic activity on Jupiter's magnetospheric dynamics. *Geophysical Research Letters*, *45*(19), 10193–10199. <https://doi.org/10.1029/2018GL079264>
- Zarka, P. (1998). Auroral radio emissions at the outer planets: Observations and theories. *Journal of Geophysical Research*, *103*(E9), 20159–20194. <https://doi.org/10.1029/98JE01323>
- Zieger, B., & Hansen, K. C. (2008). Statistical validation of a solar wind propagation model from 1 to 10 AU. *Journal of Geophysical Research*, *113*(A8). <https://doi.org/10.1029/2008JA013046>